Symbolic dynamics and periodic orbits for the cardioid billiard

1997 J. Phys. A: Math. Gen. 30 1991

(http://iopscience.iop.org/0305-4470/30/6/023)

J. Phys. A: Math. Gen. **30** (1997) 1991–2020. Printed in the UK PII: S0305-4470(97)70773-X

Symbolic dynamics and periodic orbits for the cardioid billiard

A Bäcker†§ and H R Dullin‡‖

† II. Institut für Theoretische Physik, Universität Hamburg, Luruper Chaussee 149, D-22761 Hamburg, Germany

‡ Institut für Dynamische Systeme and Institut für Theoretische Physik, NW 1, Universität Bremen, Postfach 330 440, D-28334 Bremen, Germany

Received 2 January 1996, in final form 1 November 1996

Abstract. The periodic orbits of the strongly chaotic cardioid billiard are studied by introducing a binary symbolic dynamics. The corresponding partition is mapped to a topologically well ordered symbol plane. In the symbol plane the pruning front is obtained from orbits running either into or through the cusp. We show that all periodic orbits correspond to maxima of the Lagrangian and give a complete list up to code length 15. The symmetry reduction is done on the level of the symbol sequences and the periodic orbits are classified using symmetry lines. We show that there exists an infinite number of families of periodic orbits accumulating in length and that all other families of geometrically short periodic orbits eventually get pruned. All these orbits are related to finite orbits starting and ending in the cusp. We obtain an analytical estimate of the Kolmogorov–Sinai entropy and find a good agreement with the numerically calculated value and the one obtained by averaging periodic orbits. Furthermore, the statistical properties of periodic orbits are investigated.

1. Introduction

A key step towards an understanding of the behaviour of a dynamical system is achieved by finding a symbolic dynamics. By means of the symbolic dynamics trajectories can be labelled by doubly infinite symbol sequences (see, e.g. [1–6] and references therein). Periodic orbits are represented by periodic sequences and can be systematically searched for once the coding is known. The knowledge of a complete set of a large number of periodic orbits up to a given geometric length is necessary for the application of Gutzwiller's periodic orbit theory [7], which relates the quantum mechanical density of states of the quantized billiard system to a sum over classical periodic orbits.

For hyperbolic systems the standard approach to a symbolic description is to construct a Markov partition using the expanding and contracting directions. For a non-uniform hyperbolic system there does not exist a finite Markov partition. Therefore we use a different approach based on the singularity line of the system, which yields a symbolic description with a few symbols only. However, not all symbol sequences are realized as orbits of the dynamical system; the grammar describing the admissible sequences is usually infinitely complicated. To deal with this more complicated case the idea of a pruning front

§ Present address: Universität Ulm, Abteilung für Theoretische Physik, Albert-Einstein-Allee 11, 89069 Ulm, Germany. E-mail address: baec@physik.uni-ulm.de

‖ E-mail address: hdullin@physik.uni-bremen.de

0305-4470/97/061991+30$19.50

in the symbol plane was introduced in [8]. These methods have been applied to a number of systems (see, e.g. [9–15] and references therein).

In the class of billiards inside simply connected domains of the Euclidean plane ergodic examples typically have either families of orbits accumulating in length, singularities in the boundary or non-isolated parabolic families. In the case of the cardioid billiard, which has been rigorously proven to be strongly chaotic, i.e. it is ergodic, mixing, a K-system and even a Bernoulli system [16–19], we have accumulating families and one singularity. The relation of the two in the cardioid billiard is quite interesting and a thorough understanding of their effects is a prerequisite for the semiclassical quantization of this system.

There are already several results for both, the classical and quantum mechanical cardioid billiard. The cardioid is the limiting case of a family of billiards introduced by Robnik [20], see also [21, 22] and references therein. The statistical properties of the eigenvalues of the quantized cardioid billiard were studied in detail in [23, 24]; see also [25], where the focus is on diffraction effects. A lot of work has been done on Robnik's family but the classical mechanics of the cardioid has not been analysed in depth; it is this gap we want to fill in with this work.

The paper is organized as follows. In section 2 the cardioid billiard and the billiard map are defined. We show that products of linearized maps always have a positive trace and that all orbits are maxima of the Lagrangian. Subsequently a discussion of the symmetries of the billiard map is given. In section 3 the symbolic dynamics is defined and the corresponding partition of the Poincaré section is illustrated. The initial partition is given by the discontinuity of the map. The pruning of code words is discussed in the symbol plane. In section 4 the periodic orbits are classified according to their symmetry by using the symmetry lines of the desymmetrized billiard. We give a list of the number of periodic orbits in each symmetry class up to code length 15. Families of periodic orbits with short geometric lengths and their relation to cusp orbits are investigated next. It is shown that most of them eventually get pruned. However, there remains an infinite number of families accumulating in length. In section 5 we obtain an analytical estimate for the Kolmogorov–Sinai (KS) entropy and find good agreement with the value obtained from numerical methods. The average length and the KS entropy are calculated using the periodic orbits. Finally, we investigate the statistics of periodic orbits.

2. The cardioid billiard

A billiard inside a two-dimensional Euclidean domain, Ω, is given by the free motion of a point particle inside Ω with elastic reflections at the boundary $\partial\Omega$, i.e. the angle of incidence equals the angle of reflection. The cardioid billiard is the limiting case of a family of billiards first studied by Robnik [20]. Their boundary in polar coordinates (ρ, ϕ) is given by

$$\rho(\phi) = 1 + \epsilon\cos\phi \qquad \phi \in [-\pi, \pi]. \tag{1}$$

We restrict our attention to the cardioid (see figure 1) which is obtained for $\epsilon = 1$, or implicitly by

$$F(x, y) = (x^2 + y^2 - x)^2 - (x^2 + y^2) = 0 \tag{2}$$

where $(x, y) = r(\phi) = (\rho(\phi)\cos\phi, \rho(\phi)\sin\phi)$. At $\phi = \pm\pi$ the cardioid has a singularity located at the origin $r(\pm\pi) = (0, 0)$.

From the above definition (1) we can easily derive the curvature $\kappa(\phi) = \frac{3}{4\cos(\phi/2)}$, the unit tangent vector $T = (T_x, T_y) = (-\sin(3\phi/2), \cos(3\phi/2))$, and the differential of the arc

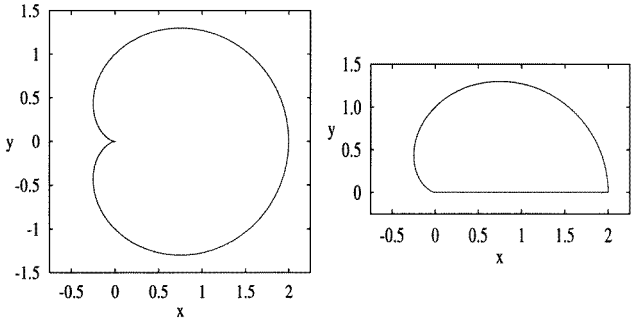

Figure 1. The full and desymmetrized cardioid billiard.

length $\frac{ds}{d\phi} = 2\cos(\phi/2)$. Thus, the arc length s is related to ϕ by $s = 4\sin(\phi/2)$. The area of the cardioid is $|\Omega| = 3\pi/2$ and its circumference is $|\partial\Omega| = 8$.

2.1. Poincaré map

We now derive the Poincaré map from bounce to bounce in coordinates $\xi = (s, p)$, where p is the component of the velocity parallel to T right after the reflection. The Cartesian components of the unit velocity v of a billiard ball starting on $\partial\Omega$ at $r(\phi)$ is determined by the angle $\beta \in [-\pi/2, \pi/2]$ measured with respect to the normal $N = (-T_y, T_x)$ pointing inward. The velocity in the T, N coordinate system is denoted by $(p, n) = (\sin\beta, \cos\beta)$, so that we obtain $v = (-\cos(\beta - 3\phi/2), \sin(\beta - 3\phi/2))$. The rightmost point of $\partial\Omega$ corresponds to arc length $s = 0$, so that the Poincaré map P is defined on the rectangle $\mathcal{P} = [-4, 4] \times [-1, 1]$. Starting at $r(\phi(s))$ in the direction $v(\phi(s), \beta(p))$, the ray $r + tv$ intersects $\partial\Omega$ at $r' = (x', y')$, which is given from the solution of a third degree polynomial derived from (2). The new s' resp. ϕ' and p' are then given by

$$\begin{aligned} \phi' &= \arctan(y'/x') \\ p' &= \sin(\beta' e) = \langle T', v' \rangle = \langle T', v \rangle = \sin(3(\phi' - \phi)/2 + \beta). \end{aligned} \tag{3}$$

The complete map $P : \xi = (s, p) \mapsto \xi' = (s', p')$ is invertible and area preserving, because s and p are canonically conjugate. For convenience we sometimes use ϕ instead of s, but without mentioning we assume it to be expressed in terms of s.

The two curves

$$\mathcal{S}_\pm = \{\xi \in \mathcal{P} | s = \pm 4\} \tag{4}$$

correspond to orbits which start in the singularity $\phi = \pm\pi$, i.e. on the right or left boundary of $\mathcal{P}$. For the image of points from $\mathcal{S}_\pm$ under P one has $\phi' = \arctan(v_y/v_x)$ because of $r = (0, 0)$. Thus, $\phi' = \pm\pi/2 - \beta$ and using equation (3) $p' = -\sin(\pm\pi/4 - \beta/2)$. The two image curves join at the origin of $\mathcal{P}$. We denote them by

$$\Gamma_\pm^{-1} = \{\xi \in \mathcal{P} | p = -s/4, \pm s \geqslant 0\} \tag{5}$$

such that $P(\mathcal{S}_\pm) = \Gamma_\pm^{-1}$. Each of the curves $\mathcal{S}_+$ and $\mathcal{S}_-$ has a fixed point $(4, -1)$ and $(-4, 1)$, respectively, which corresponds to $v_x = -1$. The physical motion starting at these fixed points is a sliding motion along the boundary, either counterclockwise or clockwise.

Note that although $r(-\pi) = r(\pi) = (0, 0)$ we take them as different points equipped with their different tangent vectors. In a differentiable point of $\partial\Omega$ one can start in directions $\beta \in [-\pi/2, \pi/2]$. In singular points this interval can be different; in our case at $r = (0, 0)$

we can go in any direction. Points starting with $v_y > 0$ are attached to $\phi = \pi$, the ones with $v_y < 0$ belong to $\phi = -\pi$. The unique point with $r = (0, 0)$, $v = (1, 0)$ in phase space can be assigned either of the two coordinates $(4, 1)$ or $(-4, -1)$ in $\mathcal{P}$. This is only a coordinate singularity and P correctly maps both points onto the same point $\xi = (0, 0)$, where the images of $\mathcal{S}_\pm$ meet. Strictly speaking the map P is defined on a rectangle with these two opposite corners identified.

Two other special lines in $\mathcal{P}$ are its upper and lower boundary

$$\mathcal{F}_\pm = \{\xi \in \mathcal{P} | p = \pm 1, s \neq \pm 4\}. \tag{6}$$

Note that $\mathcal{F}_\pm$ are half open intervals. $\mathcal{F}_\pm$ defines starting points outside of the singularity with a velocity parallel to T, i.e. $\beta = \pm\pi/2$, $p = \pm 1$. All the points of $\mathcal{F}_\pm$ are fixed points of the map, although physically they correspond to the above mentioned sliding motion.

Reversing the velocity on Γ^{-1} (omitting the index $\pm$ refers to both lines) we define the line

$$\Gamma = \{\xi \in \mathcal{P} | p = s/4\} \tag{7}$$

which is the set of initial conditions that will immediately hit the singularity. Therefore Γ^{-1} is the mirror image of Γ with respect to the s-axis. Γ is of utmost importance, because this line turns out to be (i) the discontinuity of the map, (ii) the boundary between our primary symbol regions and (iii) the origin of the pruning front. Γ separates two regions A and B in $\mathcal{P}$, see figure 2. We consider A and B as open sets, i.e. without the lines $\mathcal{F}_\pm$, $\mathcal{S}_\pm$ and Γ.

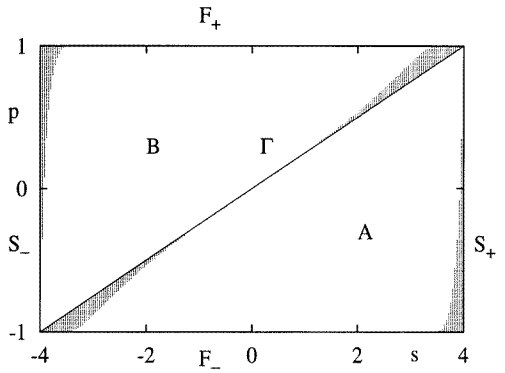

Figure 2. The regions A and B separated by Γ in the Poincaré section together with the fix lines $\mathcal{F}_\pm$ and the singularity lines $\mathcal{S}_\pm$. The shaded regions correspond to four intersections of the line $r + tv$ with the boundary $\partial\Omega$. In the white regions there are only two intersections.

In order to understand the 'kneading properties' of P we need to know the behaviour of P near Γ. Since P is discontinuous on Γ there are two different limits of P on Γ. Orbits starting in the shaded region in figure 2 will reflect off the boundary very close to the cusp while orbits on the other side of Γ just miss the cusp. We denote the corresponding limit map in the shaded region by P_s and find ($\pm$ denotes the sign of s) $P_s(s, s/4) = (\pm 4, \pm 1 - s/2)$. On the other side of Γ the limit map is $P_f(s, s/4) = (-(\pm 4 - s), (\pm 4 - s)/4)$. In figure 3 the kneading property is illustrated. Here the lines $\overline{14}$ and $\overline{56}$ map according to P_f, while $\overline{85}$ and $\overline{43}$ map by P_s.

Since the map is discontinuous at Γ, the image of Γ under the Poincaré map is not well defined. Moreover, there is no unique tangent vector in $\mathcal{S}$, because the boundary curve is not differentiable in this point. Note that we can assign the coordinate $s' = \pm 4$, but we

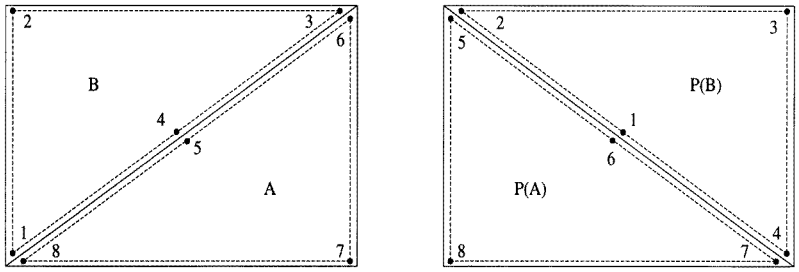

Figure 3. Demonstration of the kneading property of the billiard map. The left picture shows the regions A and B which are mapped by P to give the picture on the right-hand side. P 'kneads' triangle B by sliding point 4 to the lower right corner, while in turn point 1 is taken to the middle. The remaining points 2 and 3 stay fixed. Note that the former centre 4 becomes a corner and vice versa for 1. In a similar way A is deformed under P, by taking 5 to the upper left corner, and moving 6 to the middle. The mapping P thus contracts in the direction of Γ, and expands along Γ^{-1}.

cannot specify p' for $\xi \in \Gamma$. One might be tempted to define the image of Γ according to its limit under P_f, because also the corresponding tangent vector in $\mathcal{S}_\pm$ can be defined by an appropriate one-sided differentiation. This is, however, misleading as we will see in the discussion of finite orbits starting and ending in $\mathcal{S}$.

If we consider the desymmetrized billiard, see figure 1, the corresponding billiard map $\tilde{P}$ defined on $\tilde{\mathcal{P}} = \{\xi = (s, p) | s \in [0, 4],\ p \in [-1, 1]\}$, is obtained by first using P for a given $\tilde{\xi} \in \tilde{\mathcal{P}}$; if $\xi' \in \tilde{\mathcal{P}}$ we have $\tilde{\xi}' = \xi'$, otherwise $\tilde{\xi}' = (-s', -p')$.

2.2. Linearized map

For an arbitrary billiard the linearized Poincaré map from ξ_1 to ξ_2 can be expressed as (see, e.g. [26])

$$DP_{21} = \begin{pmatrix} 1/n_2 & 0 \\ 0 & n_2 \end{pmatrix} \begin{pmatrix} k_1 - 1 & -l \\ (k_1 + k_2 - k_1 k_2)/l & k_2 - 1 \end{pmatrix} \begin{pmatrix} n_1 & 0 \\ 0 & 1/n_1 \end{pmatrix} \tag{8}$$

where $k_i = l\kappa_i / n_i$ and κ_i and n_i denote the curvature and normal component, respectively, and l is the geometric length between the two reflections. For a periodic orbit this reduces to the more familiar form for the monodromy matrix (see, e.g. [27]).

We will now show that every periodic orbit has positive trace (in this statement and for the rest of this section we exclude $\mathcal{F}$). The argument is along the lines of Wojtkowski's pioneering work [16], but we will use a slightly different form due to Wittek [28], who applied it to the wedge billiard. We now prove that DP_{21} always has the following checker board structure

$$\begin{pmatrix} + & - \\ - & + \end{pmatrix}. \tag{9}$$

Note that the product of two checker board matrices is again a checker board matrix. Since $n_i \geqslant 0$ and $l > 0$ we need to show $k_i > 1$ and

$$\frac{1}{k_1} + \frac{1}{k_2} < 1. \tag{10}$$

Because of $\kappa_i > 0$ we have $k_i > 0$ and therefore (10) implies $k_i > 1$. Evaluating the trace with these inequalities we find that $\mathrm{Tr}\, DP_{21} > 2$, where equality would hold for $k_1 = k_2 = 2$.

Following [16] we introduce a matrix norm

$$\varrho\begin{pmatrix} a & b \\ c & d \end{pmatrix} = \sqrt{ad} + \sqrt{bc} \tag{11}$$

such that $\varrho(M_1 M_2) \geqslant \varrho(M_1)\varrho(M_2)$ if M_i has the above checker board structure and $\det(M_i) = 1$. If inequality (10) holds we have $ad > 1$, such that $\varrho(M_i) > 1$. Therefore we have $\varrho(M) > 1$ for the monodromy matrix M of a periodic orbit and reversing the argument we obtain $\operatorname{Tr} M > 2$ such that every periodic orbit is direct hyperbolic if (10) holds.

Starting from the explicit description of the Poincaré map in the previous section it seems quite hard to obtain (10) because the solution of a cubic equation is involved. Therefore we now look at the generating function of our map (see [29] for a review), which is just the length between successive reflections at $r(\phi_1)$ and $r(\phi_2)$. Note that in order to obtain the area preserving map P in coordinates $\xi = (s, p)$ we should parameterize by s_1 and s_2. However, the calculations are more conveniently done with $l(\phi_1, \phi_2)$. Denoting by $L = L(\phi_1, \phi_2) = r(\phi_2) - r(\phi_1)$ the vector joining the two reflection points,

$$l(\phi_1, \phi_2) = |L(\phi_1, \phi_2)| = 2\sqrt{\sin^2\Delta(\cos^2\Delta + 2\cos\Phi\cos\Delta + 1)} \tag{12}$$

where $\Phi = (\phi_1 + \phi_2)/2$ and $\Delta = (\phi_1 - \phi_2)/2$. The unit velocity is given by $v = L/l$ and we obtain $n_1 = \langle N_1, v\rangle$, $n_2 = -\langle N_2, v\rangle$ and thus

$$k_i = \pm l^2\kappa_i/\langle N_i, L\rangle = 3\frac{\cos^2\Delta + 2\cos\Phi\cos\Delta + 1}{2\cos^2\Delta + 3\cos\Phi\cos\Delta + 1 \pm \sin\Phi\sin\Delta} \tag{13}$$

where $+$ and $-$ correspond to k_1 and k_2, respectively. Finally

$$\frac{1}{k_1} + \frac{1}{k_2} = \frac{2}{3}\frac{2\cos^2\Delta + 3\cos\Phi\cos\Delta + 1}{\cos^2\Delta + 2\cos\Phi\cos\Delta + 1} = 1 - \frac{4}{3l^2}\sin^4\Delta < 1 \tag{14}$$

proves inequality (10). The geometric origin of this relation is the convex scattering property [16] of the cardioid, i.e. $\partial^2(\kappa^{-1})/\partial s^2 > 0$. There are a some very important consequences.

- The maximum number of conjugate points along a periodic orbit is given by the number of reflections. The reason for this is contained in the optical interpretation of (10) already described by Wojtkowski [16]: there is enough time between successive reflections in order for a conjugate point to occur. Since for a free motion there cannot be more than one conjugate point, the above statement follows.
- The eigenvalues of the monodromy matrix of periodic orbits are always positive, i.e. all periodic orbits are direct hyperbolic. Combining this with the fact that the maximal number of conjugate points of a periodic orbit equals the number of reflections, and since our map is a twist map (the upper left entry in DP_{21} is always negative), we conclude that periodic orbits are *maxima* of the Lagrangian $\mathcal{L} = \sum l(\phi_{i-1}, \phi_i)$ [29, 30]. Thus, the numerical search for periodic orbits is very much simplified, because we do not have to find saddle points of $\mathcal{L}$ (see [27, 31] for related results).
- We can obtain an analytical estimate (from below) of the maximum Lyapunov exponent and therefore also for the KS entropy by a theorem from [16], see section 5.

Note that the second statement only holds in the non-desymmetrized system. This is one of the reasons why we think that for the cardioid it is worthwhile to study the non-reduced system. Furthermore, notice that the convex scattering property, which is the basis for all the above, does not hold for any other member of the family of billiards (1), which are therefore much more difficult.

2.3. Symmetries

The time reversal symmetry of a billiard combined with the spatial symmetry of the cardioid gives us a number of symmetry classes of orbits. We will not pass to the desymmetrized billiard map but instead do the symmetry reduction on the level of the symbolic dynamics. Here we discuss the manifestation of the symmetries in the map. In the following sections this will be translated into symbol plane.

The time reversal symmetry in phase space is expressed by $\tilde{T} : (x, y, v_x, v_y) \to (x, y, -v_x, -v_y)$ and the reflection symmetry is $\tilde{R} : (x, y, v_x, v_y) \to (x, -y, v_x, -v_y)$. The corresponding involutions of the Poincaré map are T and X, where the latter is obtained from $\tilde{T}\tilde{R}$. For T we find

$$T : (s, p) \mapsto (s, -p). \tag{15}$$

which allows for a simple expression of the inverse map as $P^{-1} = TPT$. The involution corresponding to the spatial symmetry is

$$X : (s, p) \mapsto (-s, p). \tag{16}$$

X and T are involutions: $T^2 = \mathrm{id}$, $X^2 = \mathrm{id}$, $\det T = -1$, and $\det X = -1$.

Furthermore, we have $P^{-n} = XP^nX$ and $P^{-n} = TP^nT$, and thus we define two families of involutions

$$T_n = P^nT \qquad T_n^2 = \mathrm{id} \qquad \det T_n = -1 \qquad n = \pm1, \pm2 \ldots \tag{17}$$

$$X_n = P^nX \qquad X_n^2 = \mathrm{id} \qquad \det X_n = -1 \qquad n = \pm1, \pm2 \ldots . \tag{18}$$

The fixed point sets of involutive symmetries, the so-called symmetry lines, are useful in finding symmetric periodic orbits [32] and in their classification [33]. The symmetry lines are defined by $\mathcal{T}_n = \{\xi | T_n\xi = \xi\}$ and $\mathcal{X}_n = \{\xi | X_n\xi = \xi\}$. The set $\mathcal{T}_0$ contains all the orbits starting at right angles on the boundary, while $\mathcal{X}_0$ contains all orbits starting at the rightmost point of the cardioid with arbitrary angle:

$$\mathcal{T}_0 = \{\xi \in \mathcal{P} | p = 0\} \qquad \mathcal{X}_0 = \{\xi \in \mathcal{P} | s = 0\}. \tag{19}$$

All the symmetry lines can be obtained by iterating $\mathcal{T}_0$, $\mathcal{T}_1$, $\mathcal{X}_0$ and $\mathcal{X}_1$, because [32]

$$\begin{aligned} \mathcal{T}_{2n} &= P^n\mathcal{T}_0 \qquad \mathcal{T}_{2n+1} = P^n\mathcal{T}_1 \\ \mathcal{X}_{2n} &= P^n\mathcal{X}_0 \qquad \mathcal{X}_{2n+1} = P^n\mathcal{X}_1. \end{aligned} \tag{20}$$

The equations $PT\xi = \xi$ for $\mathcal{T}_1$ do not have a solution in billiards without potential and therefore also $\mathcal{T}_{2n+1} = \emptyset$. The symmetry line $\mathcal{X}_1 = \{\xi | PX\xi = \xi : (-s', p') = (s, p)\}$ corresponds to orbits that intersect the x-axis at right angles. Therefore we introduce the suggestive notation

$$\mathcal{X}_{2n}^{>} \equiv \mathcal{X}_{2n} \qquad \mathcal{X}_{2n+1}^{|} \equiv \mathcal{X}_{2n+1} \tag{21}$$

related to the geometric form of the corresponding periodic orbits. $\mathcal{X}_1^{|}$ is obtained by using (3) which yields the condition $\sin(3\phi + \beta) = \sin(\beta)$ and finally

$$\mathcal{X}_1^{|+} = \{\xi | p = -\cos(3\phi/2), \phi \in [0, \pi/2]\} \tag{22}$$

$$\mathcal{X}_1^{|-} = \{\xi | p = \cos(3\phi/2), \phi \in [-\pi/2, 0]\} \tag{23}$$

because for $|\phi| > \pi/2$ we cannot cross the x-axis.

If we consider the family of billiards (1) the set $\mathcal{S}$ does become a symmetry line. In the spirit of this notation we should call it $\mathcal{X}_0^{<}$. Moreover, its preimage $P^{-1}(\mathcal{X}_0^{<}) = \mathcal{X}_{-2}^{<} = \Gamma$ and its image $P(\mathcal{X}_0^{<}) = \mathcal{X}_2^{<} = \Gamma^{-1}$ are well defined in this case. The interpretation of

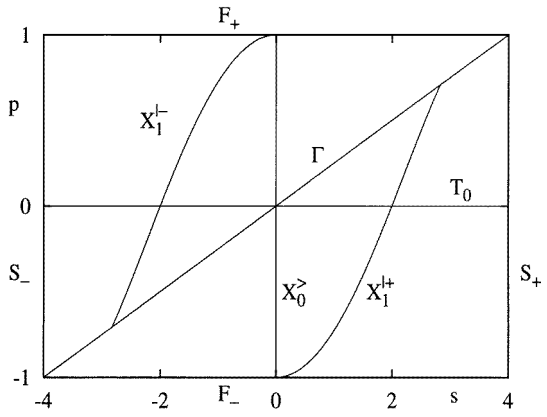

Figure 4. The symmetry lines in the Poincaré section $\mathcal{P}$. $\mathcal{T}_0$ corresponds to orbits starting at right angles on the boundary, $\mathcal{X}_0^>$ contains all orbits starting in $s = 0$, and $\mathcal{X}_1^{|\pm}$ corresponds to orbits intersecting the x-axis at right angles.

the line of discontinuity Γ as a symmetry line leads to a nice interpretation of finite orbits starting and ending in $\mathcal{S}$.

Intersections $\mathcal{X}_n \cap \mathcal{X}_m$, $\mathcal{X}_n \cap \mathcal{T}_m$ and $\mathcal{T}_n \cap \mathcal{T}_m$ of symmetry lines are periodic orbits. Intersections of symmetry lines of the same type $\mathcal{X}$ or $\mathcal{T}$ are periodic orbits with (not necessarily primitive) period $|m - n|$ [32]. If $\mathcal{X}_m$ intersects $\mathcal{T}_n$ we instead have the period $|2n - 2m|$. This is easily seen in the following way: We have $P^n T\xi = \xi$ and $P^m X\xi = \xi$, hence $P^{n-m} TX\xi = \xi$ which in turn implies $P^{2(n-m)}\xi = \xi$. After symmetry reduction we always find the period $|m - n|$.

Let us now study the intersections of symmetry lines visible in figure 4. Already the basic lines $\mathcal{T}_0$ and $\mathcal{X}_0^>$ intersect at $\xi = (0, 0)$, but the corresponding orbit is not periodic but instead a finite orbit running along the x-axis. The point $\xi = (0, 0)$ is also an intersection point of Γ and Γ^{-1}, i.e. the corresponding orbit starts on $\mathcal{S}$, is mapped to Γ^{-1} *and* Γ and back into $\mathcal{S}$ (with undefined p'). The periodic orbit with the shortest period (besides all the parabolic fixed points on $\mathcal{F}_\pm$), running vertically up and down, is given by the intersection of $\mathcal{T}_0$ and $\mathcal{X}_1^{|\pm}$ at $(\pm 2, 0)$ respectively $\phi = \pm\pi/3$. There is one more intersection in figure 4: $\mathcal{X}_1^|$ has endpoints on Γ. The (well defined) preimage of this point on Γ is on Γ^{-1}, so that this triangular-shaped orbit has two reflections besides the point in the singularity. A discussion of symmetric orbits with a higher period will be postponed until we have the symbolic dynamics at hand.

3. Symbolic dynamics

The discussion of the Poincaré map and its discontinuities suggests a natural choice for the initial partition of $\mathcal{P}$: regions A and B as separated by Γ. For a non-uniform hyperbolic system with singularities the singularity lines are a natural candidate to define an initial partition. For a given velocity on $\partial\Omega$ one can easily read its symbol as illustrated in figure 5. Transforming this description in the Poincaré section to the one in configuration space means to consider two consecutive points ϕ_1 and ϕ_2 on the boundary. If $\phi_2 > \phi_1$ the letter B is assigned for ϕ_1, if $\phi_2 < \phi_1$ we obtain A. Furthermore, we exclude the cases $\phi_1 = \phi_2$, $\phi_1 = \pm\pi$ and $\phi_2 = \pm\pi$ in order to ensure that the regions A and B correspond to open sets in $\mathcal{P}$.

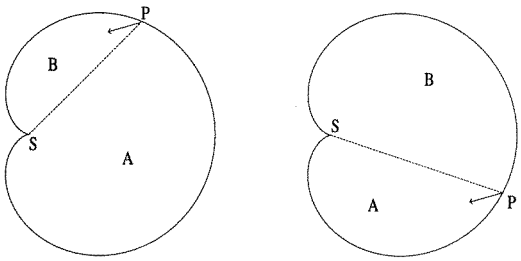

Figure 5. Examples for the determination of the symbols A and B in position space by the following rule: Connect the singularity S with the current point P. Now determine if the velocity vector is inside the sector formed by $\boldsymbol{PS}$ and the oriented tangent vector. If the velocity vector is inside the sector then B is assigned, otherwise A. In the left example, the symbol B is associated, whereas in the right example, the corresponding symbol is A.

The construction of the partition is as follows. If we superimpose Γ and Γ^{-1} we obtain four cells in $\mathcal{P}$ labelled $A.A$, $A.B$, $B.B$, and $B.A$ which are shown in figure 6. The forward image of these cells generates 'past' stripes $AA.$, $BA.$, $AB.$, and $BB.$, basically along the direction of Γ^{-1} ordered by increasing p on $\mathcal{X}_0$. The operation of P on a symbol sequence (word) just shifts the dot to the right. The sequence $AB.$ for a strip means that its preimage is in $.B$ and moreover in that part of $.B$ whose preimage is in $.A$.

The backward images of the initial cells $A.A$, $A.B$, $B.A$, and $B.B$ give stripes elongated in the direction of Γ labelled $.AA$, $.AB$, $.BA$ and $.BB$, which are just the images of the past stripes under T. The new words $.AA$, $.AB$, $.BA$ and $.BB$ tell us about the future of a given strip. The intersection of these two sets of stripes generates a partition of $\mathcal{P}$ into 2^4 cells, also displayed in figure 6; each cell is uniquely labelled by four symbols. In [34] it is shown that the images and preimages of the singularity lines are increasing/decreasing curves and that they intersect tranversally. Thus, the refinement of the partition gives a finer and finer subdivision, such that we conjecture the symbolic dynamics to be unique for the set of orbits that never hit the singularity.

3.1. Symbol plane

For any word $\alpha.\omega = \ldots s_{-2}s_{-1}.s_1s_2\ldots$ the coordinates $(\delta, \gamma) \in [0,1]\times[0,1]$ in the symbol plane (see [2, 3]) are calculated by

$$\gamma = \sum_{i=1}^{\infty} s_i 2^{-i} \qquad \delta = \sum_{i=1}^{\infty} s_{-i} 2^{-i} \tag{24}$$

where γ is the 'future' coordinate and δ is the 'past' coordinate. In the context of numerical interpretation s_i is zero (or one) for symbol A (or B).

A quite surprising observation is that for the cardioid billiard the ordering of stripes in the Poincaré section corresponds to the ordering of words (δ, γ) in the symbol plane. Thus, the symbolic dynamics is already well ordered [8, 35]. The dynamics in the symbol plane is a shift on the symbol sequences, i.e. it maps according to the baker map (see, e.g. [36]).

Figure 7 shows the onset of pruning. For symbol length 8 we have 2^8 cells, i.e. the 16 past and 16 future stripes intersect pairwise. At symbol length 10 this is no longer true. The future stripe $.AB^4$, which is the first one below Γ does not intersect the outermost past stripe $B^5.$, so that there is no cell with the label $B^5.AB^4$ (see figure 8 for a magnification of the relevant region in $\mathcal{P}$). In the magnification it is also visible that the future stripe $.BA^4$ above Γ still intersects the past stripe $B^5.$, such that the cell $B^5.BA^4$ exists.

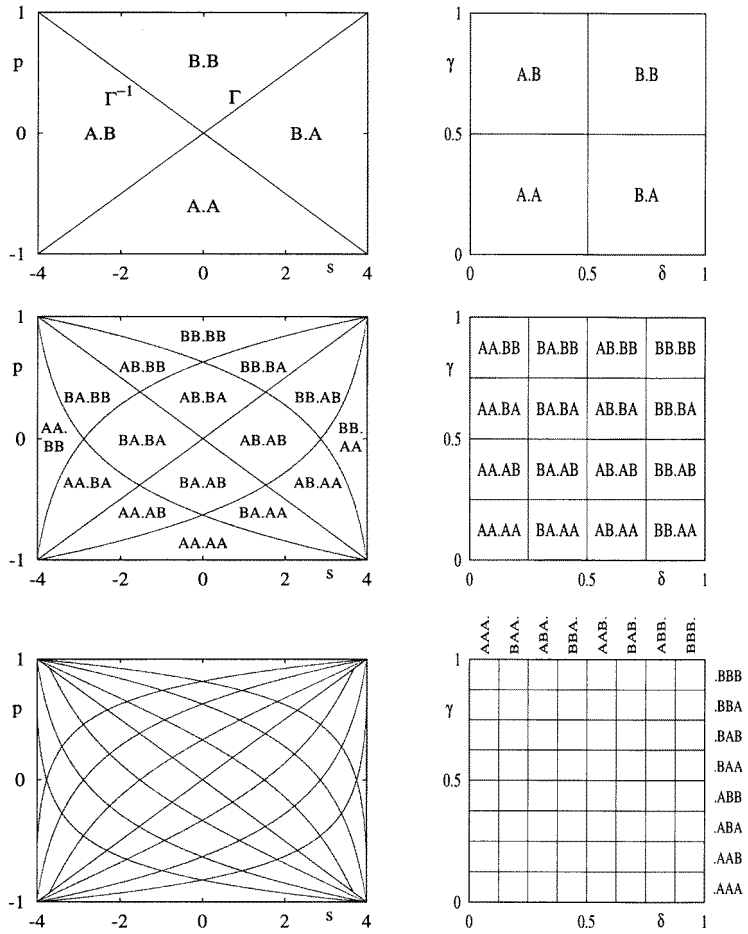

Figure 6. The division of $\mathcal{P}$ by preimages of Γ and images of Γ^{-1} into 2^2 cells with 2 symbols, 2^4 cells with 4 symbols and 2^6 cells with 6 symbols. On the right-hand side the corresponding division of the symbol plane is shown. Every line has 1, 3 or 7 intersections with other lines, respectively.

To find out systematically which cells are forbidden we plot the truncated symbolic past and future for points from a generic trajectory in the symbol plane (see, e.g. [35]). The result is shown in figure 9. The picture is symmetric under reflections with respect to the diagonals. This is caused by the underlying symmetries T, X and TX: For a word $\alpha.\omega$ the symmetry operations are realized by reading backwards $\overleftarrow{\omega}.\overleftarrow{\alpha}$ and by taking the complement $\hat{\alpha}.\hat{\omega}$. T is realized by $\hat{\overleftarrow{\omega}}.\hat{\overleftarrow{\alpha}}$, and X is represented by $\overleftarrow{\omega}.\overleftarrow{\alpha}$ alone. Thus, TX is represented by $\hat{\alpha}.\hat{\omega}$. Using equations (24) one can easily calculate the action of these operations in the symbol plane. For a given word, $\alpha.\omega$, with coordinates (δ, γ) in the symbol plane we have

$$\begin{aligned} T\alpha.\omega &= \hat{\overleftarrow{\omega}}.\hat{\overleftarrow{\alpha}} \qquad & T(\delta,\gamma) &= (1-\gamma, 1-\delta) \\ X\alpha.\omega &= \overleftarrow{\omega}.\overleftarrow{\alpha} \qquad & X(\delta,\gamma) &= (\gamma,\delta) \\ TX\alpha.\omega &= \hat{\alpha}.\hat{\omega} \qquad & TX(\delta,\gamma) &= (1-\delta, 1-\gamma). \end{aligned} \tag{25}$$

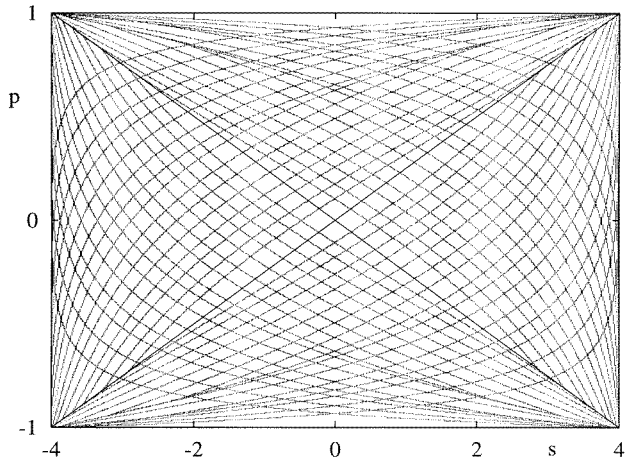

Figure 7. The division of $\mathcal{P}$ into $2^{10} - 4$ cells with 10 symbols. At this iteration level four lines have less than 31 intersections, indicating the onset of pruning.

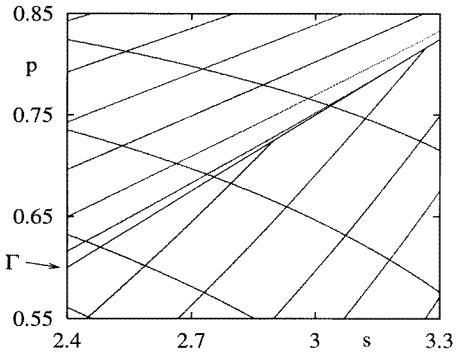

Figure 8. Magnification of figure 7. The upper right stripe is $B^5.$, the stripe above Γ is $.BA^4$, and $.AB^4$ is the one below. Since the stripes $B^5.$ and $.AB^4$ do not intersect, the sequence $B^5.AB^4$ is forbidden, whereas $.BA^4$ and $B^5.$ still intersect, such that $B^5.BA^4$ is allowed.

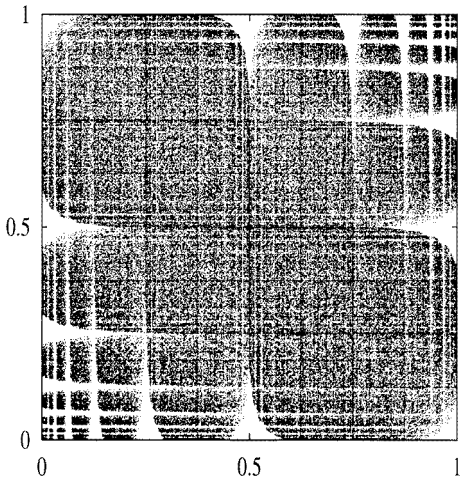

Figure 9. 10^6 iterations of a single orbit shown in the symbol plane truncated to word length 2×10.

Similarly we can define the basic symmetry lines for the symbol plane. $\mathcal{X}_0$ is given by the diagonal $\delta = \gamma$ and $\mathcal{T}_0$ is the other diagonal $\delta + \gamma = 1$.

3.2. Pruning front

Returning to the onset of pruning at word length 10 close to Γ one expects that the origin of pruning is the singularity of the cardioid. Therefore, we now study the set of symbol sequences of orbits that almost hit the singularity. Two possibilities arise: on one hand the orbit may just miss the singularity, or on the other hand, it may be reflected very close

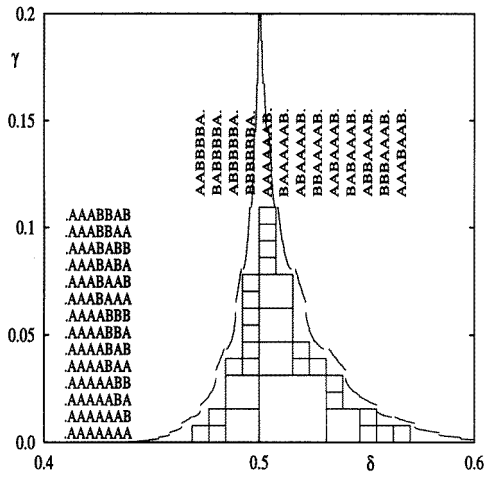

Figure 10. Magnification of the symbol plane around the primary pruning region. The s-pruning front left of $\delta = 0.5$ and the f-pruning front to the right separate allowed and forbidden code sequences. The squares of length 2^{-5}, 2^{-6} and 2^{-7} correspond to forbidden words of length 10, 12 and 14, respectively. From this one can construct the words in table 1. The part of the symbol plane that is shown corresponds to the lower right corner of the Poincaré section. The primary pruning region extends to $(0, 0.375)$ to the left, to $(0, 0.75)$ to the right and up to $(0.5, 0.5)$ to the top.

to the singularity. The limiting cases of these types of orbits generate the pruning fronts [8, 35] between allowed and forbidden sequences, see figure 10.

We think that this pruning front fulfills the conjecture stated in [8] that the region enclosed by the front and the δ-axis specifies the primary pruned region in the symbol plane. There are no orbits with a symbol sequence lying in this primary pruned region and all the other forbidden cells visible in figure 9 are related via the symmetry operations or they are images or preimages of these regions. We cannot prove that the pruning front separates allowed and forbidden orbits in the symbol plane, but we have found no counterexample.

The two pruning fronts are obtained from the two possible limiting maps P_f and P_s applied to Γ. The plan is to start with $\xi \in \Gamma$ and to use either P_f or P_s to map across the discontinuity. The corresponding symbols can be read from figures 2 and 3; if we start, for example, close to line $\overline{56}$ shown in figure 3, the current symbol is A and the application of P_f carries us into B. In the case of $\xi' \in \mathcal{S}^+$ we assign A, and for $\xi' \in \mathcal{S}^-$ we assign B. After this crucial step all further forward images under P are well defined, similarly the preimages of $\xi \in \Gamma$. Therefore an infinite symbolic past and future can be assigned to ξ and the corresponding point in the symbol plane is part of the f- or s-pruning front, depending on the initial mapping step. From the two pruning fronts in figure 10 the left with $\delta < 0.5$ is generated using P_s and will be called the s-pruning front, and the right is obtained using P_f, and will be called the f-pruning front. In the division of $\mathcal{P}$ in figure 8 the non-existing cell $B^5.AB^4$ corresponds to a square below the f-pruning front. The forbidden cells above Γ (which occur first for a division of $\mathcal{P}$ into 2^{12} cells) correspond to squares below the s-pruning front.

As a result of the above construction the two pruning fronts are related. Next we must denote by δ_s and δ_f the respective coordinates of the two pruning fronts for the same γ. We find that $\delta_f = \frac{3}{2} - 2\delta_s$. Moreover, the f-front (and the pruned region it encloses) is invariant under X_1, i.e. invariant under the map $(\delta, \gamma) \mapsto (\gamma/2 + \frac{1}{2}, 2\delta - 1)$. These symmetries in the

Table 1. Pruned words in the cardioid billiard up to length 14. The words shown $\alpha.\omega$ and additionally $\overleftarrow{\omega}.\overleftarrow{\alpha}$, $\hat{\alpha}.\hat{\omega}$ and $\hat{\overleftarrow{\alpha}}.\hat{\overleftarrow{\omega}}$ are forbidden. Code words which are already pruned by shorter words are omitted. Notice that, for example, the squares $B^5A.A^6$ and $B^5A.A^5B$ of length 12 shown in figure 10 rule out all words of the form $B^5A.A^5$ of length 11.

Word length	Pruned words ω			
10	$A^4B.A^5$			
11	$B^5A.A^5$	$A^5B.A^4B$		
12	$A^5B.A^3BA^2$	$ABA^3B.A^6$		
13	$AB^4A.A^7$	$BAB^4A.A^6$	$B^2A^3B.A^7$	$AB^2A^3B.A^6$
	$A^2BA^3B.A^5B$	$B^5A.A^4BA^2$	$B^6A.A^3BA^2$	$BA^4B.A^4BA^2$
	$ABA^4B.A^4BA$	$A^6B.A^3BAB$	$A^6B.A^3BBA$	
14	$A^3BA^2B.A^7$			

fronts induce relations between the pruned words listed in table 1. In figure 10 the pruning front is shown together with squares of length 2^{-5}, 2^{-6} and 2^{-7}. From this one can obtain finite approximations of the infinite grammar of the symbolic dynamics. The pruned words of length $10, \ldots, 14$ are given in table 1.

In figure 9 the density of points is much higher when close to the f-pruning front, while it is low when close to the s-pruning front (this is similar to the three-disk billiard [35]). The reason is that the mapping from the Poincaré section to the symbol plane is not area preserving, for example, the small cells just above Γ shown in figure 8 and the much larger ones below Γ are represented in the symbol plane by squares of the same size. Considering a generic trajectory which fills the Poincaré section uniformly, there is only a low probability in the symbol plane for squares whose corresponding cell in the Poincaré section is small.

4. Periodic orbits

Primitive periodic orbits of period n (i.e. fixed points of P^n, $P^n\xi = \xi$) correspond to periodic sequences $\bar{\omega}$ obtained from a finite word ω with n letters, where the period of $\bar{\omega}$ cannot be shortened. Two words ω and ω' belong to the same cyclic class if they can be obtained from each other by a cyclic permutation. For a periodic symbol sequence $\overline{\omega} = \overline{\omega_1 \ldots \omega_n}$, the corresponding point in the symbol plane (δ, γ) given by equations (24) becomes a geometric series and we obtain

$$\gamma = \frac{N(\omega)}{2^n - 1} = \frac{1}{1 - 2^{-n}} \sum_{i=1}^{n} \omega_i 2^{-i} \tag{26}$$

$$\delta = \frac{N(\overleftarrow{\omega})}{2^n - 1} = \frac{1}{1 - 2^{-n}} \sum_{i=1}^{n} \omega_{-i+n+1} 2^{-i} \tag{27}$$

where $N(\omega) = \sum_{i=1}^{n} \omega_i 2^{n-i}$ is the binary interpretation of ω.

The classical properties length, stability and Morse index of periodic orbits belonging to different cyclic classes, which are related by X, T or XT, are identical. Therefore, different cyclic classes will be combined into symmetry classes if their code words can be transformed into each other by reflection and/or time-reversal. As symmetry classes we define C_{full}, C_{TX}, C_{X}, C_{T}, and C_{no} using the operations defined in equation (25) (see [27, 37] for a similar classification in the case of the hyperbola billiard). Within every

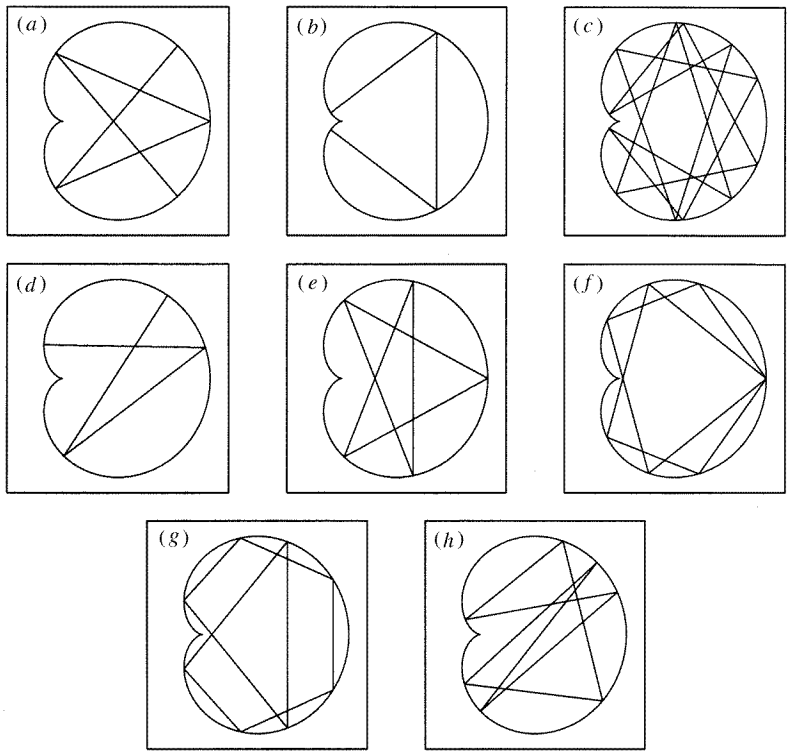

Figure 11. Examples of periodic orbits: (*a*) $\overline{AABABBAB} \in C_{\mathrm{full}}^{>\perp}$, (*b*) $\overline{AAABBB} \in C_{\mathrm{full}}^{|\perp}$ (*c*) $\overline{AAABAABBBABB} \in C_{\mathrm{TX}}$, (*d*) $\overline{AABABB} \in C_{\mathrm{T}}$, (*e*) $\overline{AABAB} \in C_{\mathrm{X}}^{|>}$, (*f*) $\overline{AAAABAAB} \in C_{\mathrm{X}}^{\gg}$, (*g*) $\overline{AAAAABAB} \in C_{\mathrm{X}}^{\parallel}$ and (*h*) $\overline{AAABABB} \in C_{\mathrm{no}}$.

symmetry class we choose the sequences with the smallest binary interpretation $N(\omega)$ as a representative for that class. To every symmetry class a multiplicity is associated, which counts the number of different cyclic classes contained in it. For C_{no} the multiplicity is 4, C_{T}, C_{X} and C_{TX} have multiplicity 2 and C_{full} has multiplicity 1. See figure 11 for some examples.

In the case of no symmetry $\leftarrow$, $\hat{\leftarrow}$ and $\hat{}$ give the symmetric partners. If $\overline{\omega} \in C_{\mathrm{T}}$ or $\overline{\omega} \in C_{\mathrm{X}}$ the corresponding symmetric partners are generated by $\leftarrow$ or $\hat{\leftarrow}$ respectively. For $\overline{\omega} \in C_{\mathrm{TX}}$ one obtains the symmetric partner by $\hat{\leftarrow}$ or $\leftarrow$, since in this case $\hat{\overleftarrow{\omega}} \equiv \overleftarrow{\omega}$. Thus, despite the fact that the orbit shown in figure 11(*c*) looks X-symmetric, application of X yields the corresponding time-reversed orbit.

The classes C_{X} and C_{full} can be subdivided with respect to the symmetry lines (see [33] for a similar discussion). We use the symbols $>$, $|$ and $\perp$ as an upper index to the class to indicate the geometric form of the orbit resulting from an intersection of the symmetry lines $\mathcal{X}^{>}$, $\mathcal{X}^{|}$ and $\mathcal{T}$. For example, subclass $C_{\mathrm{X}}^{|>} \subset C_{\mathrm{X}}$ contains orbits with period $2n-1$, that have one perpendicular intersection with the x-axis and one point with $\phi = 0$. The remaining subclasses of C_{X} are $C_{\mathrm{X}}^{\gg}$ and $C_{\mathrm{X}}^{\parallel}$, both with orbits of periods $2n$. The orbits with full symmetry can be divided into $C_{\mathrm{full}}^{>\perp}$ and $C_{\mathrm{full}}^{|\perp}$ with orbits of period $4n$ and $4n+2$, respectively. The symbol $\perp$ indicates that the corresponding orbit has two perpendicular reflections at the boundary and its $|$ or $>$ part is traversed in both directions. Orbits with T

Table 2. Number of cyclic classes, symmetry classes and the number of elements in the corresponding symmetry classes for $n = 2, \ldots, 15$ in the case of a complete binary symbolic dynamics. The number, m, of pruned orbits in the cardioid billiard is indicated by $-m$ in the corresponding classes.

			C_{full}				C_{X}			
n	Cyclic classes	Symmetry classes	$C_{\text{full}}^{\|\perp}$	$C_{\text{full}}^{>\perp}$	C_{TX}	C_{T}	$C_{\text{X}}^{\parallel}$	$C_{\text{X}}^{>\|}$	$C_{\text{X}}^{\gg}$	C_{no}
2	1	1	1	—	—	—	—	—	—	—
3	2	1	—	—	—	—	—	1	—	—
4	3	2	—	1	—	—	1	—	—	—
5	6–2	3–1	—	—	—	—	—	3–1	—	—
6	9–2	5–1	1	—	—	1	2–1	—	1	—
7	18–2	8–1	—	—	—	—	—	7–1	—	1
8	30–2	14–1	—	2	—	2	6–1	—	2	2
9	56–4	21–2	—	—	—	—	—	14–2	—	7
10	99–6	39–3	3	—	—	6	12–2	—	6–1	12
11	186–12	62–6	—	—	—	—	—	31–6	—	31
12	335–33	112–13	—	3–1	1	12–1	27–4	—	12–3	57–4
13	630–76	189–25	—	—	—	—	—	63–12	—	126–13
14	1161–145	352–46	7–1	—	1	28–2	56–10	—	28–4	232–29
15	2182–314	607–89	—	—	—	—	—	123–21	—	484–68

or TX or full symmetry are only possible for even n, since $\hat{}$ exchanges the numbers of A and B. If n is odd, only orbits from $C_{\text{X}}^{|>}$ and C_{no} exist. Elements from C_{no} only exist for $n \geqslant 7$.

In table 2 the number of cyclic classes, symmetry classes and the corresponding number of elements in the different symmetry classes are shown for $n = 2, \ldots, 15$ in the case of a complete binary symbolic dynamics. For period 1 there are two periodic sequences $\overline{A}$ and $\overline{B}$, which correspond to the lines $\mathcal{F}_{\pm}$ in our system. The shortest hyperbolic periodic orbit has period 2 and the sequence $\overline{AB}$. Due to pruning not every orbit is allowed. In table 2 the number of pruned symmetry classes are indicated by $-m$ for the corresponding symmetry classes. Starting at period 5 the orbits $\overline{A^j B}$ are pruned for $j \geqslant 4$. All other periodic code words up to period 9 correspond to physical orbits. Starting with period 9 the orbits $\overline{A^j B A^3 B}$, $j \geqslant 4$ are missing, and for period 10, in addition, $\overline{A^6 B A A B}$. Three examples of forbidden orbits are shown in figure 12.

Some of the forbidden orbits are obviously ruled out by the pruned symbols given in table 1. For example, the pruned word $A^4 B.A^5$ rules out the existence of all the periodic

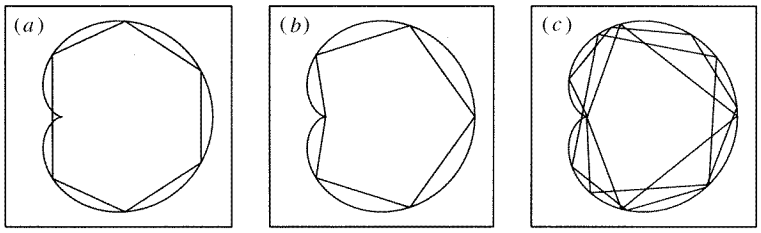

Figure 12. Examples of pruned periodic orbits: (*a*) f-pruning: $\overline{A^5 B}$, (*b*) s-pruning: $\overline{A^6 B^6}$ and (*c*) combined pruning: $\overline{A^7 B A^4 B^4}$. Note that in (*c*) the reflection in the singularity takes place only from above.

orbits of the form $\overline{A^jB}$, for $j \geqslant 5$ but not for $j = 4$. The existence of orbits cannot be deduced from the pruned words (of finite length), but only the non-existence of periodic orbits. The reason is that a periodic orbit is an infinite sequence, which might be pruned by an extremely long word which is much longer than the period. This is well illustrated in the case of the periodic orbit $\overline{A^4B}$, which is forbidden by the words $ABA^4B.A^4BA$ or $BA^4B.A^4BA^2$ of length 13, see figure 10 and table 1.

The orbit $\overline{A^5B}$ shown in figure 12(a) is an example of an f-pruned orbit. In fact, the corresponding point in the symbol plane is inside the pruned square $A^4B.A^5$, see figure 10. As an example for s-pruning in figure 12(b) the forbidden orbit $\overline{A^6B^6}$ is shown, which is pruned by the word $B^5A.A^5$, whose square is below the s-pruning front. In addition there are also orbits for which combinations of both pruning mechanisms occur, see figure 12(c).

Long orbits, especially the s-pruning, are the reason for some numerical difficulties in deciding whether an orbit has a reflection next to the cusp or whether it is pruned. Some periodic orbits close to the cusp have quite large eigenvalues, due to the fact, that the curvature diverges near the cusp. For example, for period 11 the most unstable orbit has eigenvalue 663 393 and the eigenvalue for the most unstable orbit of period 15 is even larger than 1 000 000. Note that such large instabilities cannot be calculated accurately using the monodromy matrix of the map because of rounding-off errors; therefore we use the method described in [30].

4.1. Desymmetrized cardioid billiard

The code word in the desymmetrized system can be easily read from the code word in the full system in the following way: if two adjacent symbols are identical, assign 0, otherwise 1. For example the code for $\overline{AAAB}$ in the desymmetrized systems is $\overline{0011}$. Periodic orbits of the full system with full or TX symmetry are reduced in length by a factor of 2. For example $\overline{AAABBB} \in C_{\text{full}}$ maps to $\overline{001001} \equiv \overline{001}$, or $\overline{AAABAABBBABB} \in C_{\text{TX}}$ in the desymmetrized system is given by $\overline{001101001101} \equiv \overline{001101}$.

Likewise the code word in the full system is constructed from the one in the desymmetrized system. If the code word in the desymmetrized system has an odd number of 1's, the period is doubled because otherwise it would not give a periodic word. These orbits are just the ones with C_{full} or C_{TX} symmetry in the full system.

The multiplicities of orbits in the desymmetrized system can be determined from the symmetry of the corresponding orbit in the full system: for an orbit from C_{full} the multiplicity is still 1; in the case of C_{X} and C_{T} the multiplicity reduces from 2 to 1. Orbits from C_{TX} and C_{no} are almost indistiguishable in the desymmetrized system, they both have multiplicity 2. For the relation between the code length n in the full and n' in the desymmetrized system and the corresponding multiplicities m and m' the rule $\frac{nm}{n'm'} = 2$ holds. If $n/n' = 2$ then also the geometric length and the stability exponent (which is the natural logarithm of the larger eigenvalue of the monodromy matrix M) are divided by 2.

The sign of the trace of M changes with every reflection at the x-axis. The total number of reflections at the x-axis is equal to the number of 1's in the code word of the desymmetrized system. To understand this fact it is helpful to interpret the symbols 0 and 1 in the reduced system.

In the reduced Poincaré section $\tilde{P}$ the symbol 0 corresponds to all points ξ with $|p| > s/4$, and 1 corresponds to all points with $|p| < s/4$ (again excluding $\mathcal{S}$ and $\mathcal{F}$). Notice that the region corresponding to 0 is not simply connected. In configuration space this translates to the rule illustrated in figure 13. For $s \leqslant 4/\sqrt{3}$ all orbits from the sector 1 immediately reflect at the x-axis. For $s > 4/\sqrt{3}$ only part of these orbits hits the x-axis.

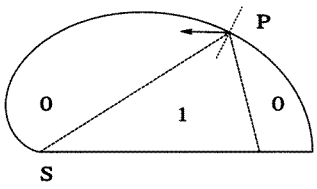

Figure 13. The rule for the symbols 0 and 1 in the desymmetrized billiard in configuration space: Connect the cusp with the current point on the boundary. Then reflect this line at the normal vector in the current point. If the actual velocity vector is in the sector formed by these two lines assign the symbol 1, otherwise 0.

The other part with negative p encounters a reflection with the boundary $\partial\Omega$ which gets it closer to $s = 0$. All the remaining reflections of this part get the symbol 0, i.e. they must eventually approach $s = 0$ and hit the x-axis before the next symbol 1 can occur.

The fact that the number, $\#_1(\omega)$, of 1's in the code word gives the number of reflections with the x-axis is important for calculating the Morse index which enters into the Gutzwiller trace formula. For a billiard system the Morse index ν is twice the number of reflections at the boundary with Dirichlet boundary condition plus the maximal number μ of conjugate points [38]. For the desymmetrized cardioid billiard in the case of Dirichlet boundary conditions $\nu = 2n + n + 2\#_1(\omega)$ and in the case of Neumann boundary conditions on the x-axis $\nu = 2n + n$. Alternatively the additional phase due to $\#_1(\omega)$ can be interpreted as coming from a group character of the underlying symmetry group. This point of view is more appropriate when dealing with more complicated group symmetries (see e.g. [39]).

The relation between the code for the desymmetrized billiard and the symmetry classes is obtained using the symmetry lines. Therefore, we first consider the relation between a symbol string and the symmetry lines $\mathcal{X}_0^>$, $\mathcal{X}_1^|$ and $\mathcal{T}_0$ in the desymmetrized system [33]. The line $\mathcal{X}_0^|$ corresponds to all points in $\tilde{\mathcal{P}}$, whose symbol sequence is symmetric with respect to the dot

$$\mathcal{X}_0^| \simeq \{\beta.\overleftarrow{\beta}\}. \tag{28}$$

The line $\mathcal{X}_1^>$ corresponds to all points in $\tilde{\mathcal{P}}$, whose symbol sequence is symmetric with respect to 0

$$\mathcal{X}_1^> \simeq \{\beta.0\overleftarrow{\beta}\}. \tag{29}$$

The line $\mathcal{T}_0$ corresponds to all points in $\tilde{\mathcal{P}}$, whose symbol sequence is symmetric with respect to 1

$$\mathcal{T}_0 \simeq \{\beta.1\overleftarrow{\beta}\}. \tag{30}$$

Iterating the basic symmetry lines $\mathcal{X}_0^>$, $\mathcal{X}_1^|$ or $\mathcal{T}_0$ shifts the point of symmetry to the left or right. Combinations of these symmetries yield the structure of the code words of periodic orbits in the symmetry classes shown in table 3.

Now the structure of the code words for a given symmetry in the full system can be determined from the structure of the code words for the desymmetrized system. The result is summarized in table 4. Notice that if one constructs code words with arbitrary α of the form given for C_X, C_{TX} or C_T, it is possible to obtain a code word with higher symmetry. Furthermore, it is possible to obtain a code word which is not primitive. The only symmetry class which is not incorporated into the above scheme using the symmetry lines are orbits from C_{TX}. The reason is that their code in the desymmetrized system does not have any

Table 3. Form of the code words for periodic orbits in the desymmetrized system.

	$\vert$	$>$	$\perp$
$\vert$	$\beta\overleftarrow{\beta}$	$0\beta\overleftarrow{\beta}$	$1\beta\overleftarrow{\beta}$
$>$	$0\beta\overleftarrow{\beta}$	$0\beta0\overleftarrow{\beta}$	$1\beta0\overleftarrow{\beta}$
$\perp$	$1\beta\overleftarrow{\beta}$	$1\beta0\overleftarrow{\beta}$	$1\beta1\overleftarrow{\beta}$

Table 4. Form of the code words for symmetric periodic orbits of the full cardioid billiard. Y and Z stand for an arbitrary single letter, α for an arbitrary word.

$C_{\mathrm{full}}^{\vert\perp}$	$C_{\mathrm{full}}^{>\perp}$	C_{T}	$C_{\mathrm{X}}^{\parallel}$	$C_{\mathrm{X}}^{>\vert}$	$C_{\mathrm{X}}^{\gg}$
$\alpha\hat{\overleftarrow{\alpha}}\hat{\alpha}\overleftarrow{\alpha}$	$\alpha Y\hat{\overleftarrow{\alpha}}\hat{\alpha}\hat{Y}\overleftarrow{\alpha}$	$\alpha\hat{\overleftarrow{\alpha}}$	$Y\alpha Z\overleftarrow{\alpha}$	$\alpha Y\overleftarrow{\alpha}$	$\alpha\overleftarrow{\alpha}$

of the symmetries, such as orbits from C_{no}. The only difference between them is that orbits from C_{no} have an even number of 1's, whereas orbits from C_{TX} have an odd number of 1's in the desymmetrized code. Thus, for a given code length orbits from C_{TX} in the desymmetrized system occur much more often than their number in table 2 for the full billiard might suggest. Actually, in the reduced system orbits from C_{TX} are even more frequent than those from C_{no}.

4.2. Families of short periodic orbits

We call a periodic orbit a short orbit if the ratio of the geometric length to the number of reflections is small compared with the average value of this ratio for the given period. Of

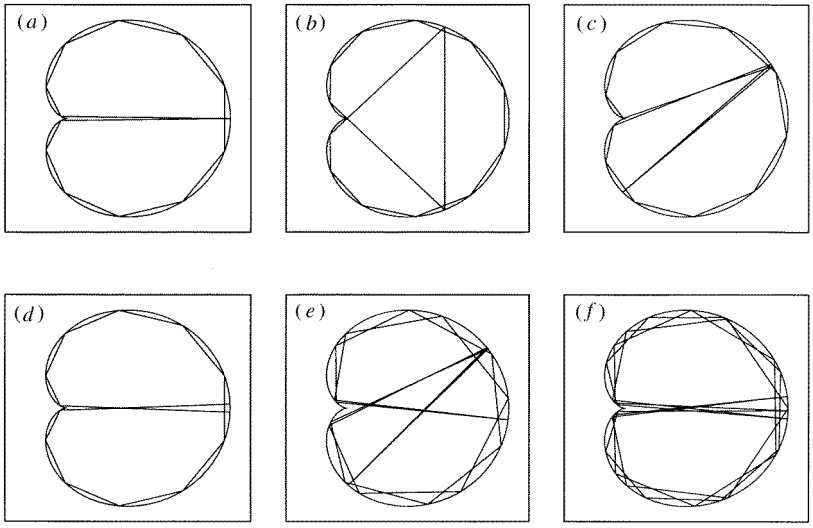

Figure 14. Examples of members of some families of short periodic orbits (*a*) $\overline{A^nBB} \equiv \overline{G_n}$ for $n = 11$, (*b*) $\overline{A^nBBB}$ for $n = 11$, (*c*) $\overline{A^nBABB}$ for $n = 11$, (*d*) $\overline{A^nBAB^mAB} \equiv \overline{G_nF_m}$ for $n = m = 11$, (*e*) $\overline{A^nBABAB^mAB}$ for $n = 7, m = 6$, (*f*) $\overline{A^9B^2A^7BAB^6AB} \equiv \overline{G_9G_7F_6}$.

special interest for the application of Gutzwiller's periodic orbit theory [7] are families of short periodic orbits where this ratio approaches zero, i.e. the orbits accumulate in length. The code words of the simplest type of families have the form $\overline{A^n\omega}$, with ω starting and ending in B. One family corresponds to fixed ω and varying n. Some examples are shown in figure 14. The family of orbits $\overline{A^nBB}$ yields the shortest accumulation length $l = 12$. Moreover, this is the only family of the form $\overline{A^n\omega}$ with finite ω, which exists for arbitrary n. All the other families of short orbits of this kind are not accumulating but instead are pruned for a finite $n > n_{\max}$. This is easily seen using the representation of the families in the symbol plane. The coordinates of $\overline{A^n\omega}$ in the symbol plane are

$$\gamma_n = \frac{N(A^n\omega)}{2^{n+m}-1} = \frac{1}{2^{n+m}-1}N(\omega) \tag{31}$$

$$\delta_n = \frac{N(A^n\overleftarrow{\omega})}{2^{n+m}-1} = \frac{2^n}{2^{n+m}-1}N(\overleftarrow{\omega}) \tag{32}$$

and thus $\lim_{n\to\infty}(\delta_n, \gamma_n) = (\delta, 0)$ with $\delta = 2^{-m}N(\overleftarrow{\omega})$. Furthermore, it turns out that all the points (δ_n, γ_n) lie on straight lines

$$\gamma_n = \frac{N(\omega)}{N(\overleftarrow{\omega})}(2^m\delta_n - N(\overleftarrow{\omega})). \tag{33}$$

By shifting the code word or by considering a symmetric partner it is possible to obtain $\delta \in]0.375, 0.75]$. If different words fulfill this criterion the one with the smallest distance to $\delta = 0.5$ is chosen. In figure 15 some examples are shown together with the pruning front. From the figure one can read the last allowed orbits as well as the pruning mechanism. If $\delta \in]0.375, 0.5[$ the family is s-pruned, whereas for $\delta \in]0.5, 0.75[$ the family is f-pruned. Applying a similar rule to the three symmetric images of the fundamental pruning region, shows that it can occur that a family is pruned by both mechanisms.

We observe that the pruning front is a monotonously increasing curve in the interval $[0.375, 0.5]$, and monotonously decreasing for $[0.5, 0.75]$. Moreover, it only reaches 0 at 0.375 and 0.75. Therefore, families of *any* kind can only exist if at least one of their limit points in the symbol plane is $(0.75, 0)$. In particular the family $\overline{A^nBB}$ exists for any n.

One can construct a variety of more complicated families, e.g. with the structure $\overline{A^n\alpha A^m\beta}$ or $\overline{A^n\alpha B^m\beta}$, see figure 14. The special case $\overline{A^nBAB^nAB}$, see figure 14(*d*),

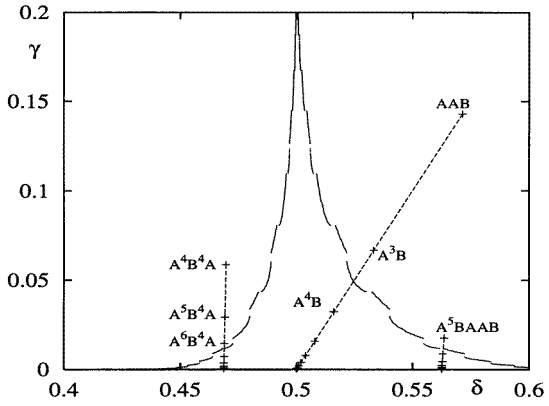

Figure 15. Sequence of points (δ_n, γ_n) in the symbol plane of some families of short orbits $\overline{A^n\omega}$ that are pruned together with the pruning front. The labels denote the corresponding shifted code word of the first plotted member.

has the accumulating length $l = 24$ and exists for any n, because the corresponding limit point in the symbol plane is $(0.75, 0)$. Actually we think that there is an infinite number of accumulating families. They can be constructed by introducing two combined symbols $F_n = AB^nA$ and $G_m = BA^mB$. Now *any* sequence of F_n's and G_m's gives an accumulating family, as long as all the indices collectively go to infinity. One example with different n_i is shown in figure 14(*f*). The length of the limit orbit of such a family is given by the total number of the symbols F_n and G_m multiplied by 12.

The instability of periodic orbits from accumulating families grows with increasing period, because they must come arbitrarily close to the cusp. However, their instability grows much slower than for generic orbits because they also get arbitrary close to the parabolic lines $\mathcal{F}$.

The pruning in the families of short orbits is related to the limiting orbit which almost hits the cusp. It consists of a sliding motion and of a finite orbit hitting the cusp as illustrated in figure 14. We now turn to the study of these finite orbits.

4.3. Finite orbits

In the quantum mechanical billiard problem discontinuities of derivatives of the billiard map can play an important role (see, e.g. [40–42] and [25, 43–46] and references therein). In the case of the cardioid billiard the singularity leads to the existence cusp orbits, which we consider as finite orbits.

They start at an arbitrary angle in the cusp and eventually return to the cusp with an arbitrary angle without the need to fulfill any reflection condition in the cusp. We think that the investigation of orbits having a reflection in the cusp is already important from the classical point of view: on one hand due to the connection to short periodic orbits and on the other hand because cusp orbits are also extrema of the Lagrangian, as it is the case for periodic orbits. This can be seen in the following way: the variation of the Lagrangian $\mathcal{L} = \mathcal{L}(\phi_1, \ldots, \phi_n)$ yields a system of n-coupled nonlinear equations $\nabla\mathcal{L} = 0$. A short calculation shows that if $\phi_i = \pm\pi$ the corresponding equation

$$\left.\frac{\partial\mathcal{L}}{\partial\phi_i}\right|_{\phi_i=\pm\pi} = \left.\frac{\partial l(\phi_{i-1},\phi_i)}{\partial\phi_i} + \frac{\partial l(\phi_i,\phi_{i+1})}{\partial\phi_i}\right|_{\phi_i=\pm\pi} = 0 \tag{34}$$

is fulfilled regardless of the values of ϕ_{i-1} and ϕ_{i+1}. This means that there is no reflection condition to fulfill in the point $\phi_i = \pm\pi$. Thus, in some sense the singularity looks like an infinitely small circle, i.e. it can reflect into any direction. Notice that the above argument does not hold if we look at $\mathcal{L}$ as a function of s_i. This dependency of the Lagrangian on the choice of coordinates is due to the singularity. We will not consider cusp orbits as periodic orbits, but instead as finite orbits with the same initial and final point in configuration space. Numerically these orbits can either be found by a one-dimensional search in the Poincaré map or by finding the stationary points the Lagrangian with fixed initial and final point.

In order to classify the cusp orbits we extend the symbolic dynamics with a third letter, C, which corresponds to the lines $\mathcal{S}$ and Γ. For a cusp orbit starting in $\mathcal{S}$, the next point lies on Γ^{-1}, from which one iterates until the image point first lies on Γ. Since the momentum is not defined in the next step we consider cusp orbits as finite orbits whose code word is $C\alpha C$, where α is a code word consisting of A and B. One could omit the C's, but we find it more convenient to have the number of letters in a code word correspond to the number of reflections. Thus, the shortest cusp orbit, which runs along the symmetry line has the code CC, because it starts in $\mathcal{S}$ and has its next and last point on Γ, see figure 16(*a*).

Since the partition of the Poincarè section as shown in figures 6 and 7 is given by the

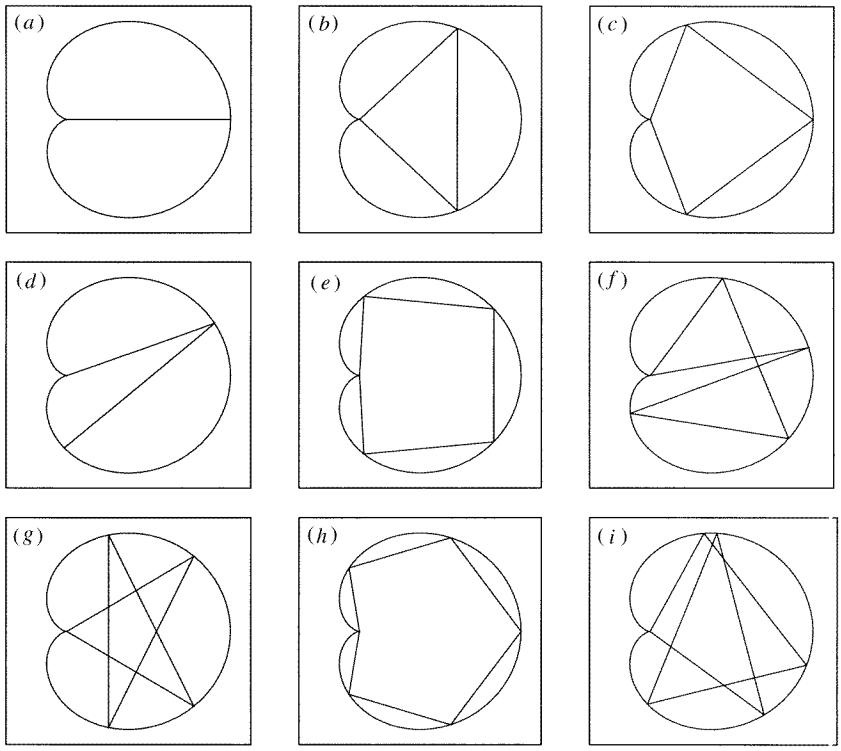

Figure 16. Examples of finite orbits (*a*) CC, (*b*) CAC, (*c*) $CAAC$, (*d*) $CABC$, (*e*) $CAAAC$, (*f*) $CAABC$, (*g*) $CABAC$, (*h*) $CAAAAC$ and (*i*) $CAABAC$.

iterates of Γ, cusp orbits correspond to the intersections of these lines. Actually it is simplest just to iterate Γ^{-1} and to look for intersections with Γ. After n iterations we have $2^{n+1}-1$ intersections (ignoring pruning), i.e. at every iteration there are 2^n new intersections, which is exactly the number of cusp orbits one expects without pruning. Defining $\Gamma^{-n-1} = P^n\Gamma^{-1}$, the number of reflections of a cusp orbit which is given by the intersection of Γ^{-n-1} and Γ, is $n+2$.

Similar to the case of periodic orbits, finite orbits can be classified according to their symmetry using the symmetry lines. Intersections of $\mathcal{T}_0$ and Γ^{-n} correspond to T-symmetric cusp orbits which have period $2n$ because the distance to Γ and Γ^{-1} is $n-1$ forward respectively backward iterations. Intersections of $\mathcal{X}_0$ and Γ^{-n} yield X-symmetric cusp orbits. In the same way cusp orbits with $\mathcal{X}_1$ symmetry are found. Starting on a symmetry line, past and future are symmetric and thus the symmetry is reproduced in the cusp, i.e. a T-symmetric orbit retraces itself also in the cusp and a X-symmetric orbit has a X-symmetric reflection in the cusp. The exceptional period 2 cusp orbit CC has full symmetry. This is not the case for any other cusp orbit.

By counting the number of intersections of the symmetry lines and iterates of Γ (ignoring pruning) we find that there are $2^{(n-2)/2}$ symmetric cusp orbits of even period n and $2^{(n-3)/2}$ for odd n. Like in the case of periodic orbits the non-symmetric cusp orbits are the overwhelming majority for large n. For a complete symbolic dynamics the number of cusp orbits is exactly 2^{n-2}, where n is the total length of the word $C\alpha C$. So already this number grows faster than the number of periodic orbits because we do not have to consider cyclic

classes here, as has been observed in [25]. Furthermore, cusp orbits can be combined to give multiple cusp orbits. Their number can be estimated using the topological polynomial [47] for the symbolic dynamics with letters $\{A, B, CC\}$, which is $1 - 2z - z^2 = 0$, such that we obtain $h_{\mathrm{top}} = -\ln(z) = \ln(1 + \sqrt{2})$ for the topological entropy. Therefore finite orbits occur much more often than the periodic orbits for which the $h_{\mathrm{top}} = \ln 2$ in the case of a complete symbolic dynamics.

We will now briefly describe the relation between cusp orbits and the families of accumulating orbits. The families $\overline{A^n\omega}$ perform n successive reflections along the boundary, which are followed by some other reflections after which the orbit returns to the approximate sliding motion. For large n this family tends to the sliding motion plus a limiting cusp orbit. If $\overline{A^n B\alpha B}$ is the code word for the family, the corresponding cusp orbit is given by $C\alpha C$. The largest angle χ between the x-axis and the limiting cusp orbit determines the maximum number of consecutive reflections having the same letter. Only for $\chi = 0$ can a family exist for any n, otherwise we have a finite family of short orbits which do not accumulate.

5. Global properties of the billiard

In this section some global characteristics of the cardioid billiard are calculated. In the first part we obtain an analytical result for the average distance between reflections $\bar{l}$ and an analytical estimate for the KS entropy h_{KS}. The same quantities are then calculated using averages over periodic orbits, where each orbit is weighted by its stability.

We first calculate dynamical averages by iterating the billiard map. Averaging over several generic trajectories for 5×10^6 iterations we obtain for the average length between reflections $\bar{l}$ and the Lyapunov exponent, which in our case equals the KS entropy h_{KS}

$$\bar{l} \approx 1.851 \qquad h_{\mathrm{KS}} \approx 0.653. \tag{35}$$

h_{KS} is calculated according to [48], however, we use the linearized map (8). We can also calculate these quantities analytically as we will now show.

For any billiard in the domain Ω the average length is determined by the area $|\Omega|$ and circumference $|\partial\Omega|$ [48] by transforming the average over the length function $l(s, p)$ on $\mathcal{P}$ (36) into the volume of the energy shell (37)

$$\bar{l} = \int_{\mathcal{P}} l(s, p)\, \mathrm{d}\mu = \frac{1}{2|\partial\Omega|} \int_{\mathcal{P}} l(s, p)\, \mathrm{d}s\, \mathrm{d}p \tag{36}$$

$$= \frac{1}{2|\partial\Omega|} \int_{\Omega\times S^1} \mathrm{d}x\, \mathrm{d}y\, \mathrm{d}\beta = \frac{|\Omega|\pi}{|\partial\Omega|} \qquad \text{i.e. for the cardioid} \tag{37}$$

$$\bar{l} = \tfrac{3}{16}\pi^2 = 1.850\,55\ldots \tag{38}$$

where $\mathrm{d}\mu = \frac{1}{2|\partial\Omega|}\, \mathrm{d}s\, \mathrm{d}p$ is the normalized Liouville measure on $\mathcal{P}$ because $|\mathcal{P}| = 2|\partial\Omega|$. The numerical average in (35) is in good agreement with this result.

An analytical expression for a lower bound on h_{KS} was given by Wojtkowski in [16]:

$$h_{\mathrm{KS}} \geqslant \int_{\mathcal{P}} \log \varrho\, \mathrm{d}\mu \tag{39}$$

where ϱ is the matrix norm (11). Since ϱ contains the length $l(s, p)$, which is given by the root of a cubic equation we again pass to the generating function of the map $l(\phi_1, \phi_2)$. The variables are transformed by

$$s(\phi_1, \phi_2) = 4\sin(\phi_1/2) \tag{40}$$

$$p(\phi_1, \phi_2) = \langle v, T_1\rangle = \frac{\langle L(\phi_1, \phi_2), T(\phi_1)\rangle}{l(\phi_1, \phi_2)}. \tag{41}$$

Since s is independent of ϕ_2 we obtain for the Jacobian of the transformation

$$\det \frac{\partial(s,\, p)}{\partial(\phi_1, \phi_2)} = 2\cos(\phi_1/2)\left(\langle L', T\rangle - \frac{\langle L, T\rangle\langle L, L'\rangle}{l^2}\right)/l \tag{42}$$

where a prime denotes the derivative with respect to ϕ_2. Since not all combinations (ϕ_1, ϕ_2) correspond to allowed trajectories, we have to restrict the integration ranges. Moreover, we use the symmetry of the system to restrict the integration to positive ϕ_1 and obtain

$$h_{\mathrm{KS}} \geqslant \frac{1}{|\partial\Omega|}\int_0^{\pi}\int_{-\pi+\phi_1}^{\pi} \log\varrho(\phi_1, \phi_2)\det\frac{\partial(s,\, p)}{\partial(\phi_1, \phi_2)}\,\mathrm{d}\phi_2\,\mathrm{d}\phi_1. \tag{43}$$

From (8) we obtain $ad = (k_1-1)(k_2-1)$ where $k_i = l\kappa_i/n_i$. Therefore we have to evaluate the following integral

$$h_{\mathrm{KS}} \geqslant \int_0^{\pi}\int_{-\pi+\phi_1}^{\pi} \log\left(\sqrt{(k_1-1)(k_2-1)} + \sqrt{k_1k_2 - k_1 - k_2}\right)\det\frac{\partial(s,\, p)}{\partial(\phi_1, \phi_2)}\,\mathrm{d}\phi_2\,\mathrm{d}\phi_1. \tag{44}$$

The numerical evaluation of this integral gives $h_{\mathrm{KS}} \geqslant 0.633$. Even though Wojtkowski's theorem only gives a lower bound on h_{KS} this value is surprisingly close to the numerically measured value (35).

h_{KS} can also be approximated by calculating the entropy of the partition of the Poincaré section $\mathcal{P}$ into cells labelled by words of length n

$$h_{\mathrm{KS}}(n) = -\frac{1}{n}\sum_{\omega} p_\omega \ln p_\omega \tag{45}$$

where $p_\omega = \mu(\omega)$ is the size of the cell with label ω (see, e.g. [49]). Since the cell sizes in $\mathcal{P}$ are quite hard to obtain we determine them numerically in the symbol plane. This is done by calculating the probability with which each cell is visited by performing many iterations of one initial condition. Thus, we numerically approximate the invariant measure in the symbol plane by assigning a probability, p_ω, to every cell labelled by a word, ω, of length n. The sum (45) extends over all allowed cells in the symbol plane. An estimate for the topological entropy with respect to the code length is obtained by setting $p = 1/N(n)$, where the total number of allowed cells labelled by words of length n is denoted by $N(n) = \sum_\omega 1$:

$$h_{\mathrm{top}}(n) = -\frac{1}{n}\sum_{\omega} p\ln p = \frac{1}{n}\ln N(n). \tag{46}$$

For $n = 22$ we obtain $h_{\mathrm{KS}} \approx 0.66$ and $h_{\mathrm{top}} \approx \ln(1.98) \approx 0.68$. h_{KS} is smaller than h_{top}; the difference tells us how much the invariant measure on the symbol plane deviates from equipartition. The three values for h_{KS} are in the expected order $0.63 < 0.65 < 0.66$: the analytical value is a lower bound and the value obtained from the symbol plane tends to overestimate due to finite size effects.

5.1. Global properties from periodic orbits

Now we repeat the calculation of h_{KS}, h_{top} and $\bar{l}$ using periodic orbits. The main point in the calculation of these averages is that the sum in (45) can be transformed into a sum over periodic orbits of fixed length. Each cell visited by a periodic orbit γ is assigned a probability given by the inverse of the eigenvalues e^{-u_γ}, from which the invariant measure is approximated (see, e.g. [47, 50, 51]).

This approach can be illustrated by a plot of the distribution of periodic orbits in the Poincaré section (see figure 17). We observe that the distribution is not as uniform as

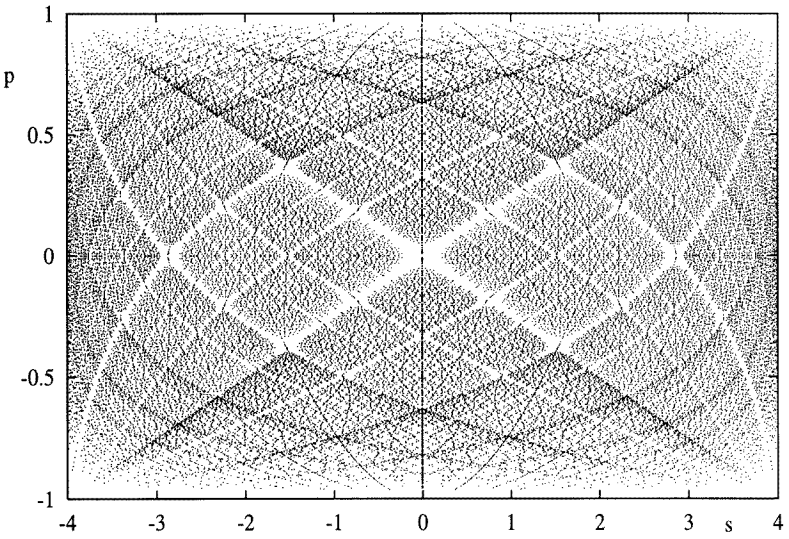

Figure 17. Plot of the points of all periodic orbits with code length up to $n = 15$ in the Poincaré section $\mathcal{P}$. The symmetry lines and the images/preimages of Γ are visible, compare with figure 4.

one might expect. Most obvious we have regions with very few periodic orbits in the neighbourhood of $\mathcal{F}$, because these orbits are rather stable. The same structure can be observed in the division of $\mathcal{P}$ into cells in figure 7. In a region where the cells are small there is a high density in contrast to regions with large cells, where the density is low. As we already discussed, the accumulating families are not only close to $\mathcal{F}$ but also close to $\mathcal{S}$ and therefore close to Γ and its images and preimages. These families evade the region surrounding Γ exactly at the points, where there exists a corresponding cusp orbit. In the neighbourhood of parts of Γ around $s \approx 2.5$ have a high density of periodic orbits. These orbits come close to Γ without having been close to $\mathcal{F}$, and are therefore extremely unstable, which is in accordance with their high density. Moreover, some of the basic symmetry lines and their iterates are visible. The reason for a relatively high density of points along the symmetry lines is the fact that they are one-dimensional. Thus, the small fraction of symmetric orbits has to fill only a 'small' set in $\mathcal{P}$, whereas the large number of orbits without symmetry has to fill large areas in $\mathcal{P}$. Plotting only orbits of a higher period makes the symmetry lines less visible. In the symbol plane the periodic orbits are much more uniformly distributed, see figure 18.

The weighted average over periodic orbits of length n of a quantity $f(u, l)$ is now given by

$$\langle f \rangle_n^w = \frac{\sum_\gamma f(u_\gamma, l_\gamma) \mathrm{e}^{-u_\gamma}}{\sum_\gamma \mathrm{e}^{-u_\gamma}} \tag{47}$$

where the sum runs over all periodic orbits γ of code length n, including multiple traversals. Although for large n we do have $\sum_\gamma \mathrm{e}^{-u_\gamma} \approx 1$ [52] we include this term for normalization.

Using the periodic orbits up to code length 20 we calculated the mean stability exponent per reflection $\langle u \rangle_n^w / n$, i.e. the Ljapunov exponent. The values approach a constant from above for increasing n with $\langle u \rangle_{20}^w / 20 = 0.657$, which agrees quite well with the value of h_{KS} in (35).

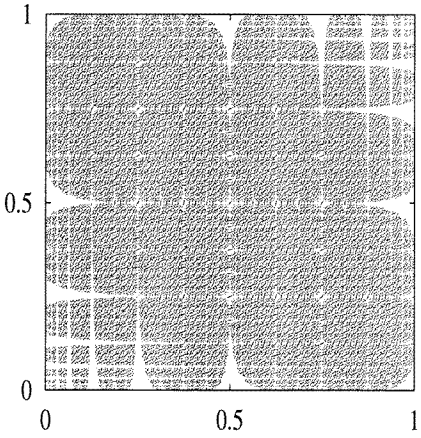

Figure 18. Plot of the points of all periodic orbits up to code length $n = 15$ in the symbol plane; compare with figure 17 where the corresponding points are presented in the Poincaré section.

For the average distance between consecutive reflections we obtain $\langle l\rangle^w_{20}/20 = 1.864$, where the values are slowly decreasing for increasing n, such that we have good agreement with the analytical result (38). The conversion of averages measured with respect to the discrete time Poincaré map and the one measured in phase space is just given by the factor (38). Thus the corresponding quantities for continuous time are given by

$$h_{\mathrm{KS}}(20)/\bar{l} = 0.36 \qquad \tfrac{1}{20}\langle u\rangle^w_{20}/\bar{l} = 0.36. \tag{48}$$

Of course $h_{\mathrm{KS}}/\bar{l}$ can also be approximated by averaging u/l which gives $\langle u/l\rangle^w_{20} = 0.363$. For the family of billiards (1) Robnik calculated the KS entropy in [20]. He gave values for ϵ close to 1, from which we extrapolate $h_{\mathrm{KS}}/\bar{l} \approx 0.34$ for the cardioid, which is consistent with our values.

Finally, we calculate the topological entropy h_{top} from the growth of the number of periodic orbits by considering $h_{\mathrm{top}}(n) = \frac{1}{n}\ln N(n)$, where $N(n)$ is the total number of points belonging to all the periodic orbits of period n, including multiple traversals. We obtain a plateau for $n \geqslant 10$ with $h_{\mathrm{top}} \approx 0.683 \approx \ln 1.98$, which is in good agreement with the value obtained in the symbol plane.

5.2. Statistical properties of periodic orbits

The following investigations are based on periodic orbits up to code length 20 (see, e.g. [27, 37, 53–55] for similar studies for other systems). The principle difference of the averages $\langle\rangle^o$ taken in this section to the averages $\langle\rangle^w$ calculated in the previous section is that now all periodic orbits are equally weighted, i.e. we have a uniform weight in the symbol plane. Thus, we transfer the picture of periodic orbits in the Poincaré section (figure 17) into the symbol plane (figure 18) and average $f(u, l)$ over periodic orbits γ of code length n by

$$\langle f\rangle^o_n = \frac{1}{N(n)}\sum_{\gamma} f(u_\gamma, l_\gamma). \tag{49}$$

Looking at figure 18 we first observe that in fact the orbits are distributed rather uniformly in the non-pruned region. The symmetry lines are almost invisible. Only the accumulating families give rise to holes that are not related to the pruning front.

In the previous section we calculated h_{top} in order to characterize the growth in the number of periodic orbits with the period. Here we study the growth behaviour of the

number $\mathcal{N}(l)$ of periodic orbits γ with geometric length l_γ below a given length l. Because the cardioid billiard is strongly chaotic one expects the typical exponential proliferation

$$\mathcal{N}(l) \sim \frac{\mathrm{e}^{\tau l}}{\tau l} \tag{50}$$

where τ is the topological entropy with respect to the geometric length of orbits. However, this classical staircase $\mathcal{N}(l)$ is not well defined in our case because of the families accumulating in length (the same happens, e.g. in the case of the stadium billiard or the wedge billiard [54]).

Therefore we define Ξ_{acc} as the set of all periodic orbits, γ, whose corresponding code has more than five consecutive letters A or B, and Ξ_{reg} as the set of periodic orbits with up to five consecutive A or B. This choice is somewhat arbitrary, but motivated by the observation that orbits from Ξ_{acc} already have the geometrical structure which is typical for the limit orbit of the considered family. We define $\mathcal{N}_{\mathrm{reg}}(l)$ as the counting function of the number of orbits from Ξ_{reg} with geometric length less than l. In figure 19 $\mathcal{N}(l)$ and $\mathcal{N}_{\mathrm{reg}}(l)$ are shown in logarithmic representation using the periodic orbits up to code length 20 together with a fit of the asymptotic behaviour (50) with $\tau \approx 0.345$. $\mathcal{N}(l)$ shows the strong increase next to $l = 12$, which is caused by the family $\overline{A^n BB}$. This step would even be more pronounced, if orbits of higher period had been used. In contrast the logarithmic plot of $\mathcal{N}_{\mathrm{reg}}(l)$ is a much 'smoother' curve, with most of these 'steps' removed.

In order to verify that the above splitting selects the accumulating families we plot the distribution $p_n(l)$ of lengths for a given code length. In figure 20(a), where all orbits with code length 14 were used, long tails down to $l = 10$ are visible. In contrast in figure 20(b) only orbits from Ξ_{reg} were used, and the outliers are removed.

We calculated the average length of periodic orbits and observed the expected linear increase of the mean length $\langle l \rangle_n^o = n\tilde{l}$ with the code length n, with $\tilde{l} = 1.99$ using all orbits and $\tilde{l} = 2.054$ using orbits from Ξ_{reg}. The variance of the distribution is also linear in n. For orbits from Ξ_{reg} we find that $\sigma_n^2 \approx \tilde{\sigma}^2 n$ for $n \geqslant 15$, with $\tilde{\sigma}^2 \approx 0.47$. Furthermore, we observed, as in the case of the hyperbola billiard [27], that $p_n(l)$ are approximately Gaussian distributed. This is demonstrated in figure 20(d) where each $p_n(l)$ is shifted to the origin and the variance is normalized.

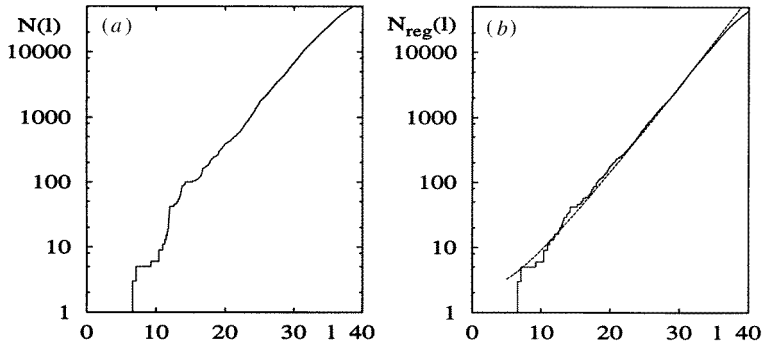

Figure 19. In (a) the logarithmic representation of the number of periodic orbits with geometric length less than l is shown using all orbits up to code length $n = 20$. In (b) $\mathcal{N}_{\mathrm{reg}}(l)$ is shown in logarithmic representation where all orbits with more than five consecutive A or B are excluded; also shown is $\frac{\mathrm{e}^{\tau l}}{\tau l}$ for $\tau = 0.345$.

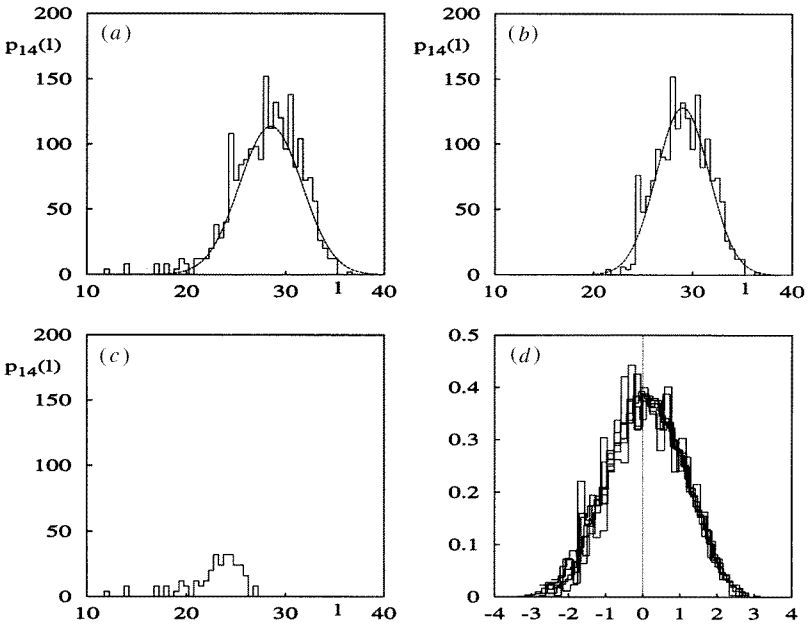

Figure 20. Probability distribution $p_n(l)$ for $n = 14$: (*a*) all orbits are included, (*b*) only orbits with not more than five consecutive A or B are used, and in (*c*) the difference between both is shown. In addition in (*a*) and (*b*) a Gaussian distribution is shown by the broken curve. In (*d*) the shifted and normalized distributions $p_n(l)$ are shown for $n = 14, \ldots, 20$ using the orbits from Ξ_{reg}.

In [27] a relation between the number of cyclic classes of code words and the classical staircase $\mathcal{N}(l)$ was derived under the assumption that $p_n(l)$ has a Gaussian distribution and that the mean length $\langle l \rangle_n^o$ and the variance σ_n^2 depend linearly on n. The result adopted to our case is

$$\tau \approx \frac{1}{\tilde{\sigma}^2}\left(\tilde{l} - \sqrt{\tilde{l}^2 - 2\tilde{\sigma}^2 h_{\text{top}}}\right) = \frac{h_{\text{top}}}{\tilde{l}} \frac{2}{1 + \sqrt{1 - 2h_{\text{top}}\tilde{\sigma}^2/\tilde{l}^2}} \tag{51}$$

where h_{top} denotes the topological entropy with respect to code words. In the case of orbits from Ξ_{reg} we obtain $h_{\text{top}} = 0.672$ and therefore $\tau \approx 0.34$, which is in good agreement with the value $\tau \approx 0.35$ obtained from the fit of $\mathcal{N}_{\text{reg}}(l)$ with the asymptotic behaviour. We take the consistency of these results as a justification of the above splitting.

We also considered the distribution of the stability exponents u_γ for fixed code length n and found that u_γ is centred around a mean $\langle u \rangle_n^o = n\tilde{u}$ with $\tilde{u} = 0.70$ using either all orbits or only orbits from Ξ_{reg}.

A further common statistic is the spacing between neighbouring lengths. In order to obtain a mean spacing of one, the asymptotic behaviour (50) is used to unfold the length spectrum. The result using orbits from Ξ_{reg} with length $l < 30$ is shown in figure 21 is in agreement with the Poisson distribution $P(s) = \mathrm{e}^{-s}$.

It is also interesting to look at the dependence of the stability exponents u_γ versus the geometric length l_γ. The result is shown in figure 22. Some of the families are clearly visible as series of points with accumulating l_γ and thereby increasing u_γ.

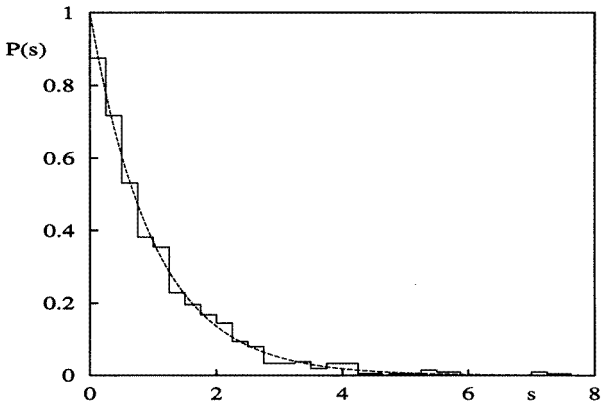

Figure 21. Length spacing distribution $P(s)$ (full line) together with the Poisson distribution e^{-s} (broken curve).

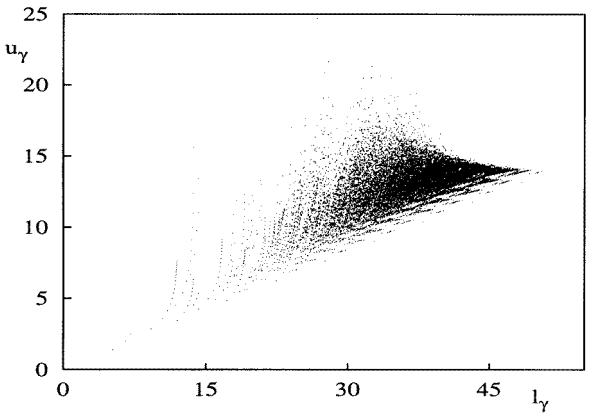

Figure 22. Plot of the stability exponents u_γ versus the geometric length l_γ using all orbits up to code length 20.

6. Summary

In this paper we have developed a symbolic dynamics for the cardioid billiard by constructing a partition of the Poincaré section $\mathcal{P}$ using two symbols A and B. After completion of the part on the symbolic dynamics a preprint appeared [25], where the same coding was found independently and used to study diffraction effects of the quantum mechanical system.

For the symbolic dynamics it turned out that not every sequence of symbols is allowed. We obtained the two pieces of the pruning front, which are related to the two pruning mechanisms in the system. Using the symbolic dynamics, periodic orbits can be labelled in a unique way. Assisted by the knowledge that all orbits correspond to maxima of the Lagrangian we calculated a large number of periodic orbits up to code length 20. Complete sets of higher-periodic orbits are hard to obtain because some of them are extremely unstable due to the unbounded curvature. Using the symmetry lines of the billiard map, we presented a classification of periodic orbits with respect to their symmetry properties. This was first obtained in the symmetry reduced symbolic dynamics and then translated back to the full

system. Combining Wojtkowski's result about convex scattering billiards with a geometric argument in the symmetry reduced system we were able to determine the Morse indices from the code words.

Studying families of periodic orbits with short geometric length provides a good application of the pruning front, because it allowed us to determine whether a family exists for arbitrary code length, or whether it is eventually pruned. In the latter case a plot of the points of the periodic orbits in the symbol plane allows for the determination of the last allowed member of the family. The converse argument enables us to write down an infinite number of families that accumulate in length. Furthermore, it turned out that cusp orbits appear rather natural even from a merely classical point of view as parts of the possible limit orbits of the short families.

In the last section we calculated an estimate for the KS entropy and found good agreement with numerically calculated values. Averaging the periodic orbits we find consistent values for the KS entropy and the average length between reflections. We illustrate the idea of the periodic orbit averaging by a plot of periodic orbits in the Poincaré section. The topological entropy is quite close to $\ln 2$ because the pruning sets in rather late.

To obtain well-defined statistics despite the presence of accumulating families we suggested a method to subtract the accumulating families. This procedure might also be helpful when using Gutzwiller's periodic orbit theory, where families of accumulating periodic orbits have to be treated separately. We believe that this method might be useful for other systems with accumulating families.

With the complete set of periodic orbits, knowledge of the Morse indices and an understanding of accumulating families and cusp orbits all the elements for the periodic orbit quantization of the cardioid billiard are available. Eventually the same program should be carried out for Robnik's family of billiards, at least close to the cardioid, where it can be expected to have large chaotic areas in phase space. On one hand, the system then lacks the singularity which makes it simpler on first sight. On the other hand we think that it becomes more difficult, because there will be inverse hyperbolic orbits, such that it is not sufficient to look for maxima of the Lagrangian in order to find periodic orbits and, moreover, a binary symbolic dynamics will not suffice.

Acknowledgments

We would like to thank P H Richter, F Steiner, A Wittek, R Aurich and T Hesse for useful comments and discussions and the referees for helpful remarks. We also thank the Deutsche Forschungsgemeinschaft for financial support under contract nos DFG-Ste 241/7-1 and DFG-Ar-137/7-6.

References

[1] Alekseev V and Yakobson M 1981 *Phys. Rep.* **75** 287–325
[2] Gutzwiller M C 1973 *J. Math. Phys.* **14** 139–52
[3] Gutzwiller M C 1976 *J. Math. Phys.* **18** 806–23
[4] Giannoni M J and Ullmo D 1990 *Physica* **41D** 371–90
[5] Morita T 1991 *Trans. Am. Math. Soc.* **325** 819–28
[6] Morita T 1994 *Ergod. Theor. Dynam. Sys.* **14** 599–619
[7] Gutzwiller M C 1990 *Chaos in Classical and Quantum Mechanics* (New York: Springer)
[8] Cvitanović P, Gunaratne G H and Procaccia I 1988 *Phys. Rev.* A **38** 1503–20
[9] Hansen K T 1992 *Phys. Lett.* A **165** 100–4
[10] Hansen K T 1993 *Nonlinearity* **6** 753–69

[11] Hansen K T 1993 *Nonlinearity* **6** 771–8
[12] Hansen K T 1995 *Phys. Rev.* E **51** 1838–44
[13] Hansen K T and Cvitanović P 1995 Symbolic dynamics and Markov partitions for the stadium billiard *Preprint* chao-dyn/9502005
[14] Ullmo D and Giannoni M J 1995 *Physica* **84D** 329–56
[15] Tanner G, Hansen K T and Main J 1996 *Nonlinearity* **9** 1641–70
[16] Wojtkowski W 1986 *Commun. Math. Phys.* **105** 391–414
[17] Szaśz D 1992 *Commun. Math. Phys.* **145** 595–604
[18] Markarian R 1993 *Nonlinearity* **6** 819–41
[19] Chernov N I and Haskell C 1996 *Ergod. Theor. Dynam. Sys.* **16** 19–44
[20] Robnik M 1983 *J. Phys. A: Math. Gen.* **16** 3971–86
[21] Robnik M 1984 *J. Phys. A: Math. Gen.* **17** 1049–74
[22] Prosen T and Robnik M 1993 *J. Phys. A: Math. Gen.* **26** 2371–87
[23] Bäcker A, Steiner F and Stifter P 1995 *Phys. Rev.* E **52** 2463–72
[24] Bäcker A 1995 Spektrale Statistiken des quantisierten Kardioid-Billards *Diploma Thesis* Universität Hamburg
[25] Bruus H and Whelan N D 1996 *Nonlinearity* **9** 1023–47
[26] Dullin H R, Richter P H and Wittek A 1996 *Chaos* **6** 43–58
[27] Sieber M and Steiner F 1990 *Physica* **44D** 248–66
[28] Wittek A 1991 Die Quantenmechanik eines nichtintegrablen Systems *PhD Thesis* Universität Bremen
[29] Meiss J D 1992 *Rev. Mod. Phys.* **64** 795–848
[30] MacKay R S and Meiss J D 1983 *Phys. Lett.* **98A** 92–4
[31] Bunimovich L A 1995 *Chaos* **5** 349
[32] Richter P H, Scholz H-J and Wittek A 1990 *Nonlinearity* **3** 45–67
[33] Jung C and Richter P H 1990 *J. Phys. A: Math. Gen.* **23** 2847–66
[34] Liverani C and Wojtkowski M P 1995 *Dynamics Reported. Expositions in Dynamical Systems* vol 4, ed C K R T Jones, U Kirchgraber and H O Walther (Berlin: Springer) pp 130–202
[35] Hansen K T 1993 *Nonlinearity* **6** 753–69
[36] Arnold V I and Avez A 1968 *Ergodic Problems of Classical Mechanics* (New York: Benjamin)
[37] Sieber M 1991 The hyperbola billiard: a model for the semiclassical quantization of chaotic systems *PhD Thesis* Universität Hamburg, *DESY Report* DESY 91–030
[38] Creagh S C, Robbins J M and Littlejohn R G 1990 *Phys. Rev.* A **42** 1907–22
[39] Robbins J M 1989 *Phys. Rev.* A **40** 2128–36
[40] Sieber M, Smilansky U, Creagh S C and Littlejohn R G 1993 *J. Phys. A: Math. Gen.* **26** 6217–30
[41] Alonso D and Gaspard P 1994 *J. Phys. A: Math. Gen.* **27** 1599–607
[42] Aurich R, Hesse T and Steiner F 1995 *Phys. Rev. Lett.* **74** 4408–11
[43] Vattay G, Wirzba A and Rosenqvist P E 1994 *Phys. Rev. Lett.* **73** 2304–8
[44] Pavloff N and Schmit C 1995 *Phys. Rev. Lett.* **75** 61–4 (erratum 1995 *Phys. Rev. Lett.* **75** 3779)
[45] Primack H, Schanz H, Smilansky U and Ussishkin I 1996 *Phys. Rev. Lett.* **76** 1615–18
[46] Whelan N D 1996 *Phys. Rev. Lett.* **76** 2605–8
[47] Artuso R, Aurell E and Cvitanović P 1990 *Nonlinearity* **3** 325–59
[48] Benettin G and Strelcyn J-M 1978 *Phys. Rev.* A **17** 773–85
[49] Eckmann J-P and Ruelle D 1985 *Rev. Mod. Phys.* **57** 617–56
[50] Grebogi C, Ott E and Yorke J A 1988 *Phys. Rev.* A **37** 1711–24
[51] Gaspard P and Alonso D 1992 *Phys. Rev.* A **45** 8383–97
[52] Hannay J H and Ozorio De Almeida A M 1984 *J. Phys. A: Math. Gen.* **17** 3429–40
[53] Harayama T and Shudo A 1992 *J. Phys. A: Math. Gen.* **25** 4595–611
[54] Szeredi T and Goodings D A 1993 *Phys. Rev.* E **48** 3518–28
[55] Aurich R and Marklof J 1996 *Physica* **92D** 101–29